Understanding Solar Cell Contacts Through Simulations

by

Sagnik Dasgupta

A Thesis Presented in Partial Fulfillment
of the Requirements for the Degree
Master of Science

Approved November 2020 by the
Graduate Supervisory Committee:

Zachary Holman, Chair
Arthur Onno
Qing Hua Wang

ARIZONA STATE UNIVERSITY

December 2020

ABSTRACT

The maximum theoretical efficiency of a terrestrial non-concentrated silicon solar cell is 29.4%, as obtained from detailed balance analysis. Over 90% of the current silicon photovoltaics market is based on solar cells with diffused junctions (Al-BSF, PERC, PERL, etc.), which are limited in performance by increased non-radiative recombination in the doped regions. This limitation can be overcome through the use of passivating contacts, which prevent recombination at the absorber interfaces while providing the selectivity to efficiently separate the charge carriers generated in the absorber. This thesis aims at developing an understanding of how the material properties of the contact affect device performance through simulations.

The partial specific contact resistance framework developed by Onno et al. aims to link material behavior to device performance specifically at open circuit. In this thesis, the framework is expanded to other operating points of a device, leading to a model for calculating the partial contact resistances at any current flow. The error in calculating these resistances is irrelevant to device performance resulting in an error in calculating fill factor from resistances below 0.1% when the fill factors of the cell are above 70%, i.e., for cells with good passivation and selectivity.

Further, silicon heterojunction (SHJ) and tunnel-oxide based solar cells are simulated in 1D finite-difference modeling package AFORS-HET. The effects of material property changes on device performance are investigated using novel contact materials like Al0.8Ga0.2As (hole contact for SHJ) and ITO (electron contact for tunnel-oxide cells). While changing the bandgap and electron affinity of the contact affect the height of the

Schottky barrier and hence contact resistivity, increasing the doping of the contact will increase its selectivity. In the case of ITO, the contact needs to have a work function below 4.2 eV to be electron selective, which suggests that other low work function TCOs (like AZO) will be more applicable as alternative dopant-free electron contacts. The AFORS-HET model also shows that buried doped regions arising from boron diffusion in the absorber can damage passivation and decrease the open circuit voltage of the device.

ACKNOWLEDGEMENTS

The journey that has led to the completion of this thesis was not a straightforward one, and it could not have been completed without the substantial help, support, and encouragement of those around me.

I express my sincerest gratitude to my supervisor, Dr. Zachary Holman, for his constant technical guidance and insight, which directed progress towards completing this work. His direct influence has contributed substantially to my academic and professional growth.

I am also extremely grateful to Dr. Arthur Onno, who directly supervised my work on partial specific contact resistances in chapter 2. Without his hand on guidance and long, insightful discussions, both this thesis and my understanding of photovoltaics would have been rendered incomplete.

The work discussed in chapter 4 was performed in collaboration with the silicon solar cells group in NREL, Colorado. Therefore, this work would not have been possible without the scientific support of Dr. David Young and Dr. Pauls Stradins, who directly contributed to my understanding of passivated contacts based on tunneling oxides.

I also thank Dr. Shariar Anwar, who guided me during my TA position, and has continued to be a professional advisor. I further thank Dr. Peter Crozier for giving me the opportunity to join ASU as a TA in the Fall of 2018, without which I would never have been able to work on this thesis.

I am deeply thankful to Dr. Friedhelm Finger, Dr. Vladimir Smirnov, Dr. Andreas Lambertz and Dr. Katharina Welter of Forschungszentrum Jülich for seeding my interest in the field of photovoltaics.

I would extend my deepest gratitude to my close friends and lab mates Zachary Leuty and Barry Hartweg, for their unwavering support and insightful discussions, which contributed to the completion of this work. I am also grateful to my lab mates, specifically David Quispe and William Weigand, whose insights in silicon heterojunction fabrication and characterization directly contributed to the completion of this work. I especially thank Dr. Joe Carpenter for his support over the span of my research at ASU.

I also sincerely thank my roommates Ankita Roy and Saurabh Vishwakarma, and friends Shruti Sharma, Rahul Raghavan, Md. Yasir Sayyad for their constant encouragement and support and for keeping my morale high during stressful times. I particularly thank Serita Sulzman and Pranandita Biswas for their invaluable encouragement and care and for giving me confidence in my abilities.

Lastly, this work would never have been successful without the constant, unwavering, and unconditional love and support of my parents Dr. Arup Dasgupta and Sikha Dasgupta. I am truly indebted to them for listening to my live-narration of my simulations and their occasional insightful inputs. The increased frequency of simulation convergence during my phone calls with them is statistically significant.

TABLE OF CONTENTS

Page

CHAPTER Page

LIST OF TABLES

Table Page

LIST OF FIGURES

Figure Page

Figure Page

Figure Page

Figure Page

Figure Page

CHAPTER 1

INTRODUCTION

As of 2019, solar power accounts for only 2.6% of global power output. Despite this, solar energy is the fastest growing source of renewable energy with 117 GW of net power generating capacity added in 2019 alone, about twice the capacity of added wind technology[1]. This has been driven primarily by the gradual decrease in the cost of solar production. Lazard's Levelized Cost of Energy Analysis (LCOE 13.0) shows that utility-scale PV costs in the range of $32-$42 per MWh[2]. Currently, crystalline silicon photovoltaic technologies account for about 95% of this production[3].

Terrestrial crystalline silicon solar cells have a maximum theoretical power conversion efficiency (PCE) limit of 29.4%. About 30% of silicon solar cell market share is based on Aluminum back surface field (Al-BSF) solar cells, and 65% is based on passivated emitter based cells (PERC, PERL, etc.)[4]. Despite the highest efficiency research cells reaching efficiencies of 26.7%[5], the current commercially applied designs of these cells are fundamentally limited to efficiency limits of around 20% for Al-BSF and 23%-24% for PERC[6]. The fact that these limits are substantially below the theoretical limit of c-Si itself can be primarily attributed to the high non-radiative recombination arising from the direct contact of the metal electrode to the silicon absorber. This motivates the development of material interlayers that reduce recombination at the metal-semiconductor interface while still having the right work function characteristics for efficient charge carrier extraction. These layers are generally called contacts.

A good contact is expected to have efficient separation and extraction of carriers from the absorber, i.e., high carrier selectivity, as well as the ability to prevent non-radiative recombination at the interface with the absorber, i.e., high passivation. Further, it is advantageous for the contact to have high conductivity to minimize resistive losses at the maximum power point. It is important to note, moreover, that the electrical benefits of highly selective, passivating, and conductive contacts can be rendered inadequate in increasing the efficiency of solar cells if the contact parasitically absorbs a substantial amount of incoming light. This leads to an optimization problem of several materials properties of the contact like crystallinity, dopant concentration, optical absorbance, etc. which affect the performance of a solar cell.

Recent solar cells, aimed at overcoming the limits of PERC, use heterojunction contacts, i.e., layers of different bandgaps relative to the absorber. One such example is the use of a thin intrinsic layer of amorphous silicon on the absorber for passivation and another highly doped layer for carrier selectivity. Such a stack of layers is commonly referred to as a silicon heterojunction (SHJ) cell, and a variant of this technology involving interdigitated n and p contacts at the rear of the solar cell holds the current efficiency record of 26.7% for single crystal non-concentrating silicon solar cells[7].

These heterojunction contacts based on amorphous silicon layers have exceptional electrical performance but are limited by the optical properties of the contact, specifically arising from increased absorption in the wavelength range between 250 nm- 600 nm, which constitutes a significant part of the solar spectrum as shown in Fig 1. Avoiding this parasitic absorption through the utilization of interdigitated back contacts (IBCs) leads to

significantly increased cell costs. This motivates the need for novel and inexpensive contact materials which have lower parasitic absorption and electrical performance that matches or exceeds amorphous silicon contacts.

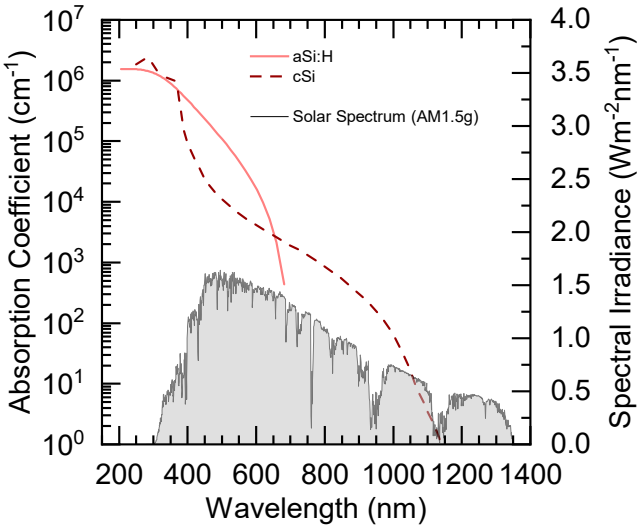

Fig. 1 Absorption coefficients of amorphous silicon[8] and crystalline silicon[9]. Solar spectrum in the same wavelength range for context[10]. In the region of visible light, where terrestrial spectral irradiance is significant, the absorbance of amorphous silicon is high.

Recently materials like MoO_x[11], LiF_x[12], TiO_x[13,14], etc. have been widely acclaimed for their ease of deposition (typically through thermal evaporation or sputtering) and excellent optical properties, making them candidates for replacing aSi:H contacts. These novel contact materials are typically characterized and compared using the measurement of specific contact resistance (ρ_c)[15] through TLM, and recombination current ($j_{0,c}$)[16] which is a metric of interface recombination as it is extracted from lifetime measurements. This is sometimes called the lumped skin model of a contact[17]. Such characterization of a contact does not, however, account for selectivity. In fact, there is no widely agreed upon framework for quantifying carrier selectivity.

Onno et al. have proposed a unified framework of partial specific resistances of the contacts[18] with broader applicability over other models for contact selectivity[19,20]. However, this model was built to only describe the solar cell at open circuit. In *chapter 2* of this thesis, I show that it is possible to use this partial specific contact resistance framework as a proxy for overall solar cell performance. This involves extending the work of Onno et al. beyond open circuit through simulations in PC1D. The goal of this chapter is to propose the partial specific contact resistances as parameters that can be fully indicative of the performance of the contact in the solar cell, taking passivation, carrier selectivity, and contact conductivity into account.

Having a fundamental model of contact behavior is not sufficient for understanding the effects of material property changes in device performance. For instance, changing the doping of the aSi:H layers in heterojunction cells will change the selectivity of the contact[21], while changes in the work function of the transparent conducting oxide (TCO) on the front of the device will determine if the contact is ohmic or a Schottky barrier[22]. *Chapter 3* looks at the effect of such changes in material properties on device performance through simulations in AFORS-HET[23]. While this is explored from the perspective of aSi:H contacts, this leads to insights on general trends that can be expected from changes in similar material properties in more novel contact materials.

Apart from aSi:H based heterojunction cells, the other major upcoming cell technology is in the form of tunnel-oxide passivated contacts (TOPCON). These devices use an ultra-thin tunneling silicon oxide layer for passivation with a doped poly-Si layer as a selective contact[24]. Utilizing the insights gained in *chapter 3,* in *chapter 4,* I show the

implementation of a double-side passivated TOPCON cell in AFORS-HET. Further, I apply this model to explore the viability of replacing the front poly-silicon layer (which contributes significantly to parasitic absorption), with an ITO electron contact. I also investigate the effects of buried doped regions in the absorber, which form due to the diffusion of boron during annealing steps in the fabrication of TOPCON devices[25].

CHAPTER 2

PARTIAL SPECIFIC CONTACT RESISTANCES AS AN INCLUSIVE PROXY FOR SOLAR CELL PERFORMANCE

2.1 Introduction: Understanding Contacts

Solar cells generate electricity by absorbing incoming radiation and generating charge carriers that are then extracted as current across a voltage difference. However, for the carriers that are generated in the absorber to be efficiently extracted, they need to be collected at spatially separated contacts at either side of the absorber[26]. Furthermore, there must be a concentration difference between electrons and holes at either contact. If the concentrations of both carriers at a given contact are similar, it will lead to non-radiative recombination at the interface where the carriers are collected[27]. This necessitates the existence of a mechanism to selectively separate the charge carriers spatially from the point of generation to the point of collection.

Classically, in a p-n junction solar cell, the electric field in the space charge region is thought to affect the separation of the charge carriers to their respective terminals[16]. This school of thought is, however, incorrect. Due to a finite conductivity in the semiconductor, the field will have to do work to move the carriers, for which there is no energy source. Further, device structures where there is charge carrier separation without the influence of electric field are theoretically possible[28].

A more physically consistent explanation that will be discussed in this chapter would be to consider that the charge carriers are driven by the gradients in the quasi-fermi levels. While this would be consistent with the popular approach involving the need for an electric field for charge carrier separation, this is insufficient for selective collection of carriers at

either contact. A more complete understanding of carrier transport at the contacts can be derived from the quasi Fermi level gradients and the local conductivities to each type of carrier at the given contact[28]. In fact, this conductivity based approach to contacts can explain a variety of phenomena, like selectivity, passivation, and series resistance[18].

As mentioned earlier, a symmetric p-n homojunction solar cell is typically introduced as the prototype for the functioning of a solar cell due to its structural simplicity. In practice, however, this device structure is modified for optimal performance. Typically, one of the layers is much thinner than the other but more highly doped, resulting in an asymmetric space charge region. The reason for this will be discussed in further detail later. On the other side of the device, aluminum is diffused into the silicon to aid in carrier transport and ensure an ohmic contact. This is known as an aluminum diffused junction solar cell and, as previously stated, is currently the industry standard[29]. As suggested in *chapter 1*, it can be beneficial to performance to use materials of different bandgaps, making a junction with silicon, resulting in silicon heterojunction solar cells. This was first demonstrated by Sanyo/Panasonic in 2000 by using amorphous silicon contact layers, resulting initially in a 20.1% efficient solar cell[30]. Materials and structure improvements and optimization over the last two decades have led to a current efficiency record for this kind of device at 26.7%[7]. While we will not be discussing this device specifically, results from this chapter will be useful in understanding this class of solar cells.

2.2 Fundamental Physics of Solar Cells

2.2.1 Structure of a solar cell

Fundamentally, a solar cell consists of an absorber, layers to impart carrier selectivity, and metallization. Electron and hole pairs are generated in the absorber layer and diffuse towards the contacts due to carrier concentration gradients, which lead to local slope in the quasi-Fermi level. The contacts are high or low work function materials that help the separation of charge carriers for collection, as will be discussed in section 2.2.3. These layers (especially the front contact) should have low absorbance to ensure that the incoming light reaches the absorber. Further, in practical solar cells, there are transparent conductive oxides like ITO used for lateral transport. Fig 2a shows such a structure.

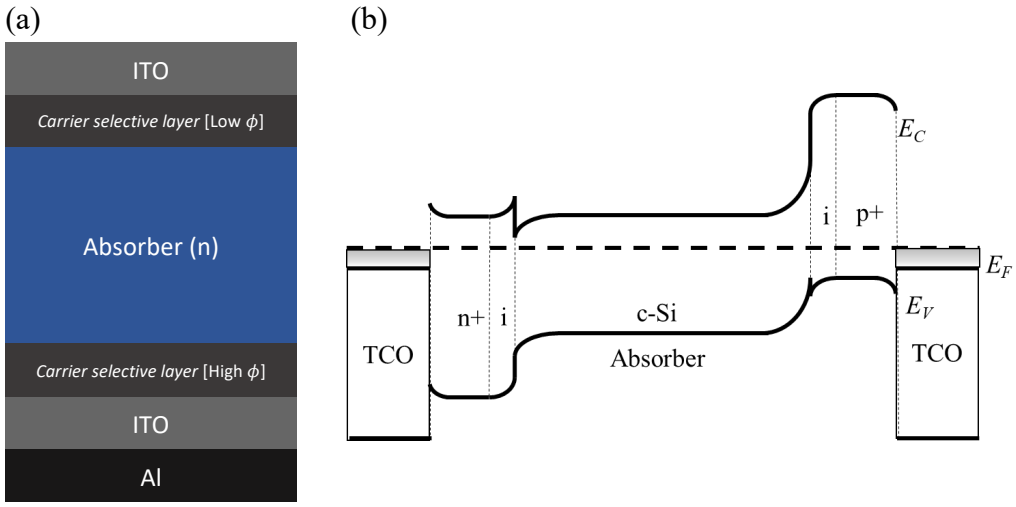

Fig. 2 a) General structure of a heterojunction solar cell with two carrier selective layers. The high work function layer is the hole selective contact, and the low work function layer is the electron selective contact. The ITO layers are for lateral transport and to improve light trapping.; b) Band diagram of an SHJ cell. Here the n doped a-Si is the electron contact, and the p a-Si is the hole contact.

2.2.2 Generation and Recombination

When a photon enters the solar cell, it can be either absorbed, reflected, or transmitted. In classic cell structures, with full rear metallization, it is almost impossible for transmission to happen. Reflection will lead to loss of photons. Ideally, we would want all incoming photons to be absorbed in the absorber layer. Absorption in any other layer is called parasitic absorption. These processes are represented in the absorption plot of the device, as shown in Fig. 3 generated in TU Delft's GenPro4[31].

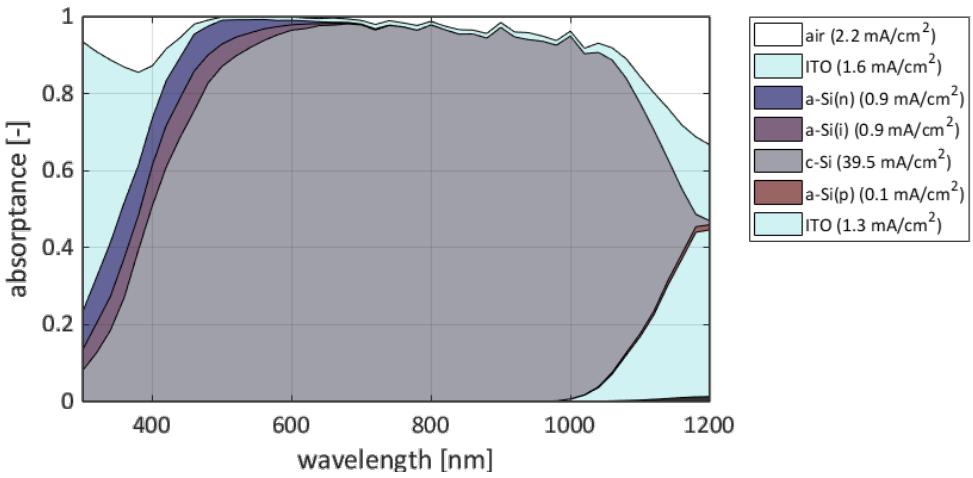

Fig. 3 Absorption plot of a Silicon heterojunction solar cell generated in GenPro4. The figure shows absorption of all the layers on a stacked plot. Also labeled are the current densities associated with the absorption at short circuit. The current density of the c-Si layer is the JSC of the cell. The remaining currents represent the current loss due to parasitic absorption. Note that here, the "absorption" in air is technically the loss due to reflection.

If the energy of a photon that is absorbed in the absorber exceeds the bandgap, it will generate an electron-hole pair. This generated electron-hole pair is, however, not stable and will recombine given enough time (usually a few milliseconds in silicon). This generated electron hole-pair can recombine radiatively and emit a photon of energy equal to the bandgap. This photon can be reabsorbed to generate another electron-hole pair. Therefore, this process is not unfavorable. In fact, for an efficient solar cell, this radiative recombination process is necessary to approach the theoretical efficiency limit[32].

An electron-hole pair can also recombine non-radiatively. In the Shockley Read-Hall process, an electron in the conduction band loses energy due to hopping through defect states in the bandgap, releasing phonons into the crystal[33,34].

Alternatively, energy generated through radiative recombination may be absorbed by an electron in the conduction band. This electron will get excited to a higher energy level and will thermalize back to the band edge, losing its energy to phonons. This form of non-radiative recombination is called Auger recombination, and it is particularly significant in silicon due to its indirect bandgap and resultant high carrier lifetimes[35,36]. These non-radiative recombination mechanisms depend on doping of the absorber layer, as well as injection during operation.

Carriers also recombine at the semiconductor-metal interface. While this is necessary because metals cannot support quasi-Fermi level splitting, this can lead to pinning of the Fermi level at the interface due to defect states in the bandgap, which can affect carrier concentrations at the absorber-metal interface in metal back-surface field solar cells[37]. Similarly, doped semiconductor contacts used in heterojunction cells can also allow recombination at the absorber interface due to dangling bonds. To prevent this, additional passivation semiconductor layers can be used to avoid Fermi level pinning (and hence interface recombination) on the crystalline silicon surface. One solution is to plug these dangling bonds with hydrogen radicals or materials with a high concentration of nascent hydrogen. To achieve this, in SHJ cells, a thin layer of PECVD i-aSi:H is deposited and subsequently annealed. This process is known as passivation[38]. It is worth noting that sometimes, dielectric layers (like tunneling SiO_2) can also be used for passivation[39].

A metric to quantify non-radiative recombination would be minority carrier lifetime, which is a measurable parameter from which it is possible to calculate a parameter called recombination current density, which is a fairly fundamental property and can be useful for comparing absorbers in different cells and for modeling. However, cells with different thicknesses can have different performance while showing the same minority carrier lifetime. Alternatively, external radiative efficiency, defined as the fractional contribution of radiative recombination to the total dark recombination current of the cell[40], can be used as a metric of non-radiative recombination.

The recombination current density is defined by the diode equation. In equation (1), J_R is the current density for the recombination process being considered, J_0 is a proportionality constant derived from material parameters, q is the electronic charge, iV is the quasi Fermi level splitting in the solar cell, k_B is the Boltzmann constant, T is the temperature, and m is the ideality factor. The ideality factor is different for each recombination mechanism depending on the number of carriers involved in the process. Radiative recombination has an ideality factor of 1, i.e., the same as an ideal diode. This is because the process is limited by the minority carrier concentration. For SRH recombination, the ideality factor is two (at high injection), and for Auger recombination, it is 2/3.

$$J_{rec} = J_0 \left(1 - e^{\frac{q \cdot iV}{m \cdot k_B \cdot T}} \right) \quad (1)$$

2.2.3 Separation of charge carriers

Once the carriers are generated in the absorber, the electron-hole pair needs to be separated spatially for collection. This is done through carrier selective contacts. In a high-quality absorber, the diffusion lengths are sufficiently high for the carriers to reach their respective contacts. The contacts are designed to allow one type of carrier to pass while blocking the other.

Consider the electron contact of the cell. This layer, in an SHJ cell, is typically n-type aSi:H. The doping in this layer is substantially higher than the doping in the n type absorber layer. It has a low work function to induce band bending at the contact, as shown in Fig 2b. This band bending manifests as an accumulation of electrons and a depletion of holes at the interface. In other words, the electron contact is hole blocking.

From another perspective, the high n-type doping of the electron contact results in high electron concentration in the layer, resulting in low resistance to electrons. However, since this layer has a low hole concentration, it has a much (by several orders of magnitude) higher resistance to holes, thus blocking it. In fact, using this approach, it should be possible to create selective contacts that do not depend on doping or work function at all but are selective due to different mobilities for electrons and holes. This kind of "mobility-junction" cell was a concept developed and simulated by Würfel et al.[28] The dependence of the resistances to carrier concentration and mobility are determined by the Drude equation and will be discussed further in the next section.

A poorly selective cell will have a high proportion of carriers unable to be extracted by the contact either due to being too resistive to majority carriers or not being resistive

enough to minority carriers (resulting in increased recombination in the contact). If carriers do not reach the metal layers through the contacts, they will not contribute to the output voltage of the device. Looking at the device at open circuit, we can infer that a device with poor selectivity will have a lower V_{OC} than a similar device with better contact selectivity. If the contacts are perfectly selective, then the open circuit voltage of the device will be equal to the steady-state quasi Fermi level splitting (known as implied voltage – iV_{OC}). Therefore, selectivity can be defined as a ratio of these voltages (as shown in equation (2)), and hence be used as a metric of the fraction of carriers that are generated but not extracted in the contacts. This concept will be revisited in the next section.

$$S = \frac{V_{OC}}{iV_{OC}} \tag{2}$$

2.3 Partial Specific Contact Resistances

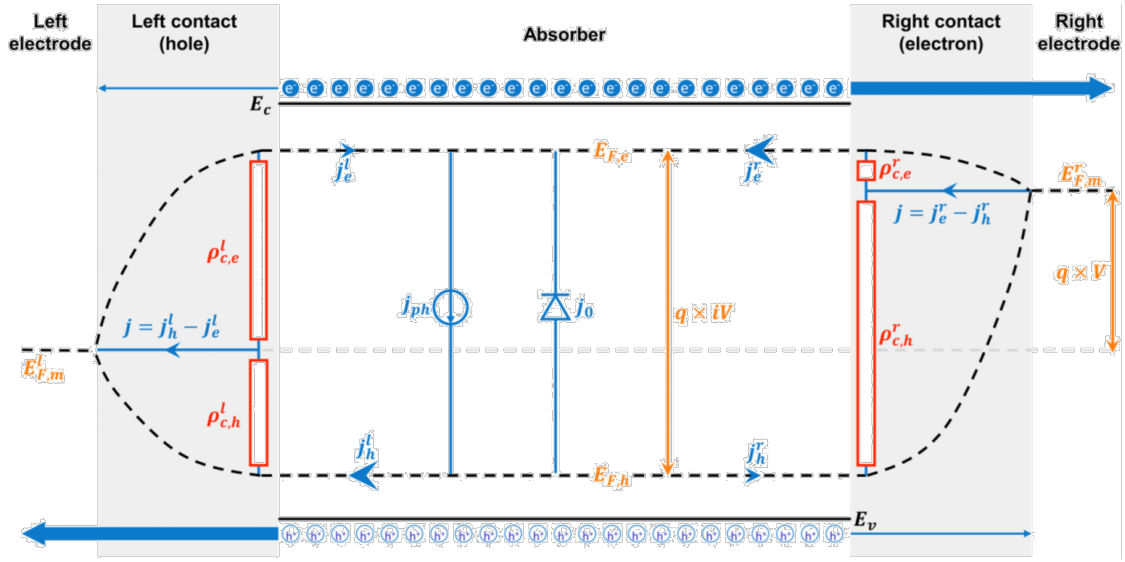

Fig. 4 Schematic quasi Fermi level diagram of the solar cell. It can be considered that the corresponding quasi Fermi level is an electrical wire for that specific carrier, carrying a partial current. Note the collapse of the quasi Fermi levels in the contacts that allow calculation of the partial specific contact resistances. (Reprinted from "Onno et al.; Passivation, conductivity, and selectivity in solar cell contacts: Concepts and simulations based on a unified partial-resistances framework. J. Appl. Phys. ***126****, 1–27 (2019)", with the permission of AIP Publishing)*

As suggested in the previous section, the selective nature of a contact can be related to the ratio of conductivities to electrons and holes. Consider the electron contact. Let j_e and j_h be the electron and hole partial current densities in the contact. Then, using the Drude formula, we get the following equations[18].

$$j_e = \frac{\sigma_e}{q}\frac{\mathrm{d}E_{f,e}}{dx} = \mu_e n \frac{\mathrm{d}E_{f,e}}{dx} \tag{3}$$

$$j_h = \frac{\sigma_h}{q}\frac{\mathrm{d}E_{f,h}}{dx} = \mu_h p \frac{\mathrm{d}E_{f,h}}{dx} \tag{4}$$

Here, σ_h and σ_e are the partial hole and electron conductivities, respectively, and $E_{f,h}$ and $E_{f,e}$ are the hole and electron quasi Fermi levels as a function of position. It is important to note that degenerate semiconductors like ITO and metals do not support separate quasi Fermi levels. This implies that the quasi Fermi levels need to collapse over the length of the contact, from maximum splitting in the absorber to no splitting in the metal. This is achieved through recombination at the contact-metal interface. This recombination, unlike other non-radiative recombination mechanisms, is unavoidable. Therefore, for good passivation it is important to prevent minority carriers from being able to reach this interface.

This collapse of the quasi Fermi level splitting in the contacts is shown in Fig. 4. Using this information, equations (3) and (4) can be integrated across the length of the contact. The contact absorber interface will be denoted by the subscript ‘c’, and the contact metal interface with the subscript ‘m’. Let ‘l’ be the thickness of the contact.

$$j_e l = \frac{\bar{\sigma}_e}{q}\left(E_{f,m} - E_{fe,c}\right) \tag{5}$$

$$j_h l = \frac{\bar{\sigma}_h}{q}\left(E_{f,m} - E_{fh,c}\right) \tag{6}$$

Using these equations, we define partial specific contact resistances as follows.

$$\rho_e = \frac{l}{\overline{\sigma_e}} = \frac{\left(E_{f,m} - E_{fe,c}\right)}{q j_e} \tag{7}$$

$$\rho_h = \frac{l}{\overline{\sigma_h}} = \frac{\left(E_{f,m} - E_{fh,c}\right)}{q j_h} \tag{8}$$

Note that here, the mobility is considered spatially constant in the contact. The same treatment can be performed for the hole contact and will result in very similar equations. So, for the sake of simplicity, in this chapter, we will focus on the electron contact.

In a hypothetical cell with an ideal hole contact, we can calculate the selectivity of the electron contact as a function of these resistances. At open circuit, $j_e = j_h$.

$$S_e = \frac{V_{OC}}{iV_{OC}} = \frac{E_{f,m}^{Right} - E_{f,m}^{left}}{E_{fe,c} - E_{fh,c}} = \frac{\rho_e}{\frac{1}{\rho_e} + \frac{1}{\rho_h}} = \frac{\rho_h}{\rho_e + \rho_h} \tag{9}$$

Alternatively, we can have the following for a hole contact when the electron contact is ideal.

$$S_h = \frac{\rho_e}{\rho_e + \rho_h} \tag{10}$$

If both contacts are non-ideal, we can calculate the overall selectivity as follows.

$$S_{Tot} = S_h^{left} + S_e^{right} - 1 \tag{11}$$

It is worth noting that the selectivity of a perfectly non-selective contact ($\rho_e = \rho_h$) is 0.5. Therefore, from equation 11 it can be seen that is both contacts are perfectly non-selective, the overall selectivity of the cell is zero. On the other hand, if both contacts are

ideal, the overall selectivity is 1. If one of the contacts is ideal, then the total selectivity of the solar cell is equal to the selectivity of the non-ideal contact. This fact is important for subsequent discussions where the hole contact is assumed to be ideal.

2.4 Solar Cell Model

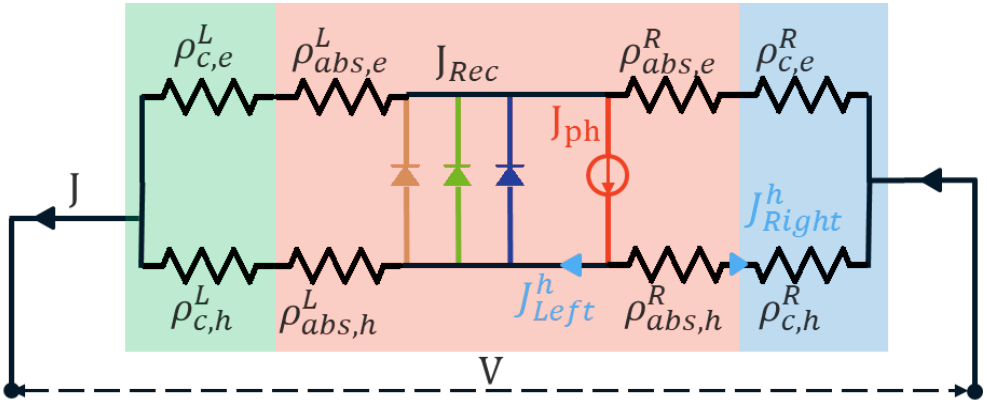

Fig. 5 The model of a solar cell described by partial resistances of electrons and holes in the absorber and the contact. J_{ph} represents the photogenerated current, and the three diodes represent, radiative (Orange), Auger (Green), and SRH (Blue) recombination, respectively. Together, the recombination currents can be combined into a single J_R recombination term by simple linear addition.

The resistances defined in the previous section allow describing the solar cell as a device with a current generator corresponding to the illumination photocurrent, a set of recombination diodes with different ideality factors, and the resistances in the contacts. It is important to note that the absorber itself has finite resistances arising from the carrier concentration in it at different injection levels, the local slope of the quasi Fermi levels, and mobility. These absorber resistances can themselves contribute to the selectivity of the contact. Using the circuit diagram shown if Fig. 5, the current voltage characteristics of the solar cell can be calculated in terms of the resistances, recombination parameters and illumination.

Since the absorber and the contact partial resistances are in series, the corresponding terms can be combined.

$$\rho_h^L = \rho_{c,h}^L + \rho_{abs,h}^L \tag{12}$$

$$\rho_h^R = \rho_{c,h}^R + \rho_{abs,h}^R \tag{13}$$

$$\rho_e^L = \rho_{c,e}^L + \rho_{abs,e}^L \tag{14}$$

$$\rho_e^R = \rho_{c,e}^R + \rho_{abs,e}^R \tag{15}$$

Using these combined resistance terms with the circuit model in Fig. 5, we get two equations.

$$\frac{(J_{ph} - J_R)\rho_e^L - V}{\rho_e^R + \rho_e^L} - \frac{(J_{ph} - J_R)\rho_h^L + V}{\rho_h^R + \rho_h^L} = J \tag{16}$$

$$(J_{ph} - J_R)\rho_e^L - \frac{(J\rho_h^R + iV)(\rho_e^R + \rho_e^L)}{\rho_h^R + \rho_e^R} = V \tag{17}$$

In these equations, iV is the implied voltage of the solar cell. This is defined by the quasi Fermi level splitting of the device and can sometimes be used as a proxy for the operating point of the device. Here, J_R is the combined recombination current term. Note the different ideality factor for each mode of recombination.

$$J_R = J_{0,rad}\left(1 - e^{\frac{q \cdot iV}{k_B T}}\right) + J_{0,\,Auger}\left(1 - e^{\frac{3q \cdot iV}{2k_B T}}\right) + J_{0,\,SRH}\left(1 - e^{\frac{q \cdot iV}{2k_B T}}\right) \tag{18}$$

Equations (16) and (17) link the resistances that define the contact to measurable device properties, specifically current, voltage, and implied voltage. Knowing these parameters for a continuous range of operating points of the device and knowing the combined resistances of either the left or the right contact reduces these expressions into a "two equations, two unknowns" system. This means that it will be possible to calculate the resistances for the other contact.

This proposition will be verified using simulations in the coming sections. For simplicity of the simulations, the left contact, i.e., hole contact of the simulated solar cell is assumed to be infinitesimally thin and ideal. This means that it has infinite resistance to electrons and zero resistance to holes. This modifies the band structure and circuit diagram, as shown in Fig 6.

(a)

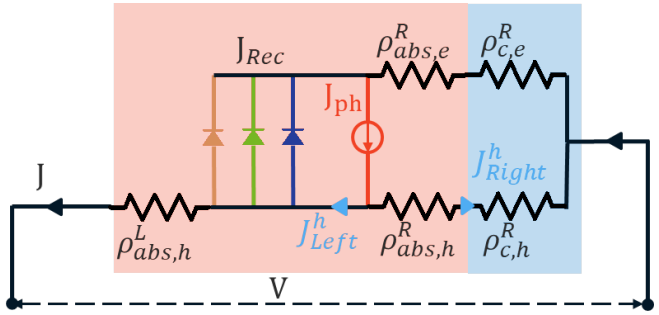

(b)

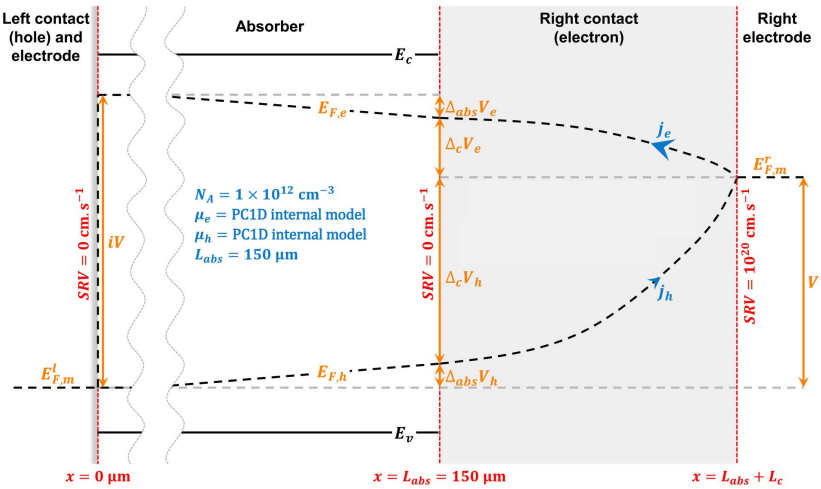

Fig. 6 (a) Schematic equivalent circuit diagram of the device being simulated with an ideal hole contact. (b) Schematic quasi-Fermi level diagram of the device under the assumption of an ideal hole contact. (Reproduced from Onno et al. 2019[18]).

Assuming the ideal hole contact, equations (16) and (17) can be changed to the following.

$$\mathrm{V} = \left(\mathrm{J_{ph}} - J_R\right)\rho_h^R - J\left(\rho_{Abs,h}^L + \rho_h^R\right) \tag{19}$$

$$\mathrm{J}\left(\frac{\rho_h^R}{\rho_h^R + \rho_e^R}\right) = \mathrm{J_{ph}} - J_R - \frac{iV}{\rho_h^R + \rho_e^R} \tag{20}$$

It is important to note that the left side absorber resistance for holes term remains as a loose end. This term cannot always be assumed to be zero because, at certain operating points of the device, it controls the hole current entering the left contact and is thus non-negligible. This suggests that a truly perfect selective contact is impossible, as the absorber's finite resistance itself will contribute to impeding the collection of carriers, even if it is minute. In practical solar cells, however, this term will be negligible compared to the resistance of the contact itself to its majority carriers. In simulations, this term will have to be calculated from the quasi Fermi level data.

2.5 Defining the Contacts

As discussed in section 2.2.1, a contact is typically defined as a layer that aids selective extraction of carriers generated in the absorber. However, treating the contact as a separate layer would be inaccurate. In the previous section, it was shown the quasi Fermi level starts collapsing in the absorber close to the contact. Therefore, there is a contribution to selective collection of carriers from a part of the absorber, implying that regions in the absorber can act as part of the contact. This is consistent with the combined (absorber + contact) resistance treatment used in the previous sections. Therefore, it would make sense to define the contact in terms of selectivity rather than material boundaries. For instance, if a region of the solar cell has a lower resistance to electrons than holes by a certain threshold, it can be considered part of the electron contact. It is important to note that this analysis must me

made with respect to the baseline ratio of electron and hole resistances in the bulk of the absorber. This approach for defining contacts is applicable to metal diffused junction solar cells where there is no separate carrier selective layer, but rather a region in the absorber with a carrier selective diffusion.

2.6 Simulations

The simulations were performed on PC1Dmod 6.2[41], an unofficial modernized revision of UNSW's widely used PC1D 5[42]. As discussed above, in the simulations, the hole contact was assumed to be ideal, i.e., infinite resistance to electrons and zero resistance to holes. The crystalline silicon absorber was set to a thickness of 150 μm with an acceptor doping of 1×10^{12} cm^{-3}. The absorber utilized PC1D's internal mobility model for Si. The electron contact was also set to have the bandgap of crystalline silicon with variable doping, thickness, and carrier mobilities. These specifics are described in Fig 6b. Monochromatic light of wavelength 1000 nm is used as illumination resulting in a total photogenerated current density (J_{ph}) of $39.25\ mA\ cm^{-2}$. The key assumptions in this simulation are that the generation rate in the absorber is uniform, and that in the rear contact is zero. While the second assumption typically holds up in most silicon solar cells, the first one is necessary for simplicity in understanding the results of the simulations. Further, the simulations assume that there is no recombination at the absorber-contact interface and that the contact-metal interface is infinitely recombination active. The latter was done by setting an absurdly high surface recombination velocity of 10^{20} cm s^{-1}.

The uniform generation assumption, along with having long diffusion lengths in the absorber, ideally ensures spatially constant quasi Fermi level splitting at equilibrium in

most of the absorber. At open circuit, this is true from the front of the solar cell to a region fairly close to the rear contact, where the quasi-Fermi level starts collapsing, i.e., the electron quasi-Fermi level monotonically decreases with depth while the hole quasi-Fermi level monotonically increases. When the device is not at open circuit, however, holes generated in the absorber will be collected at the left contact. For this left-side hole current to exist, the hole quasi-Fermi level can no longer be monotonically increasing and needs to have a minimum from which the hole currents diverge. Since the quasi Fermi level splitting in the absorber does not have a constant value, the maximum quasi Fermi level splitting will be used as the implied voltage for consistency with the results of Onno et al.[18]. This is shown in Fig. 7.

These simulations were performed for 100 cells chosen from a set of 10500. The inputs into PC1D and the simulations were controlled using MATLAB[43]. The data obtained were also extracted into MATLAB, and the resistances were calculated as described in section 2.3.

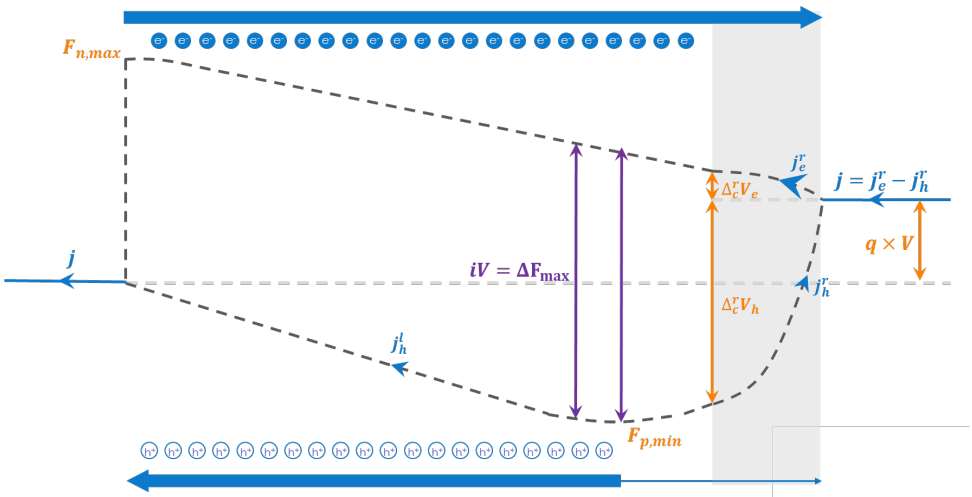

Fig. 7 The quasi Fermi level gap in the absorber is not constant when there is a flow of current in the solar cell. It is also worth noting that the maximum quasi Fermi level splitting, which is used in this chapter as the implied voltage, is not the quasi Fermi level splitting at the minimum of the hole quasi Fermi level.

Table 1 Parameters varied in PC1D

Parameter	Minimum	Maximum	Steps
$\mu_e(cm^2V^{-1}s^{-1})$	10^{-3}	10^4	7
$\mu_h\ (cm^2V^{-1}s^{-1})$	10^{-1}	10^5	6
$N_D\ (cm^{-3})$	2×10^{10}	2×10^{19}	50
$L_c\ (\mu m)$	0.1	10	5

Four parameters of the contact were varied logarithmically in the ranges shown in Table 1 to generate the initial set of 10500 cells. For silicon heterojunction cells, while the electron and hole mobilities and doping densities typically fall in the ranges considered, the amorphous silicon is usually around 10 nm thick, which is below the thickness range. However, for understanding the behavior of a representative model of a solar cell, these parameters are sufficient. From these 10500 points, four prototypes were chosen to represent a near-ideal cell, a cell with a poorly conductive contact, one with a poorly passivating contact, and one with poor selectivity. Their corresponding parameters are shown in Table 2. Aside from these, for each of these parameters, the maximum, minimum, and median were chosen as points of interest resulting in 81 cells. The remaining 19 were selected from a uniform distribution of the 10500 points.

Table 2 The four prototype cells

	$\mu_e(cm^2V^{-1}s^{-1})$	$\mu_h\ (cm^2V^{-1}s^{-1})$	$N_D\ (cm^{-3})$	$L_c\ (cm)$
Good Cell	46.41589	1.584893	4.45×10^{17}	1×10^{-3}
Poor Conductivity	0.001	1.584893	2.91×10^{17}	3.16×10^{-4}
Poor Selectivity	0.014678	1.584893	6.18×10^{13}	1×10^{-3}
Poor Passivation	10000	25.11886	9.43×10^{13}	1×10^{-3}

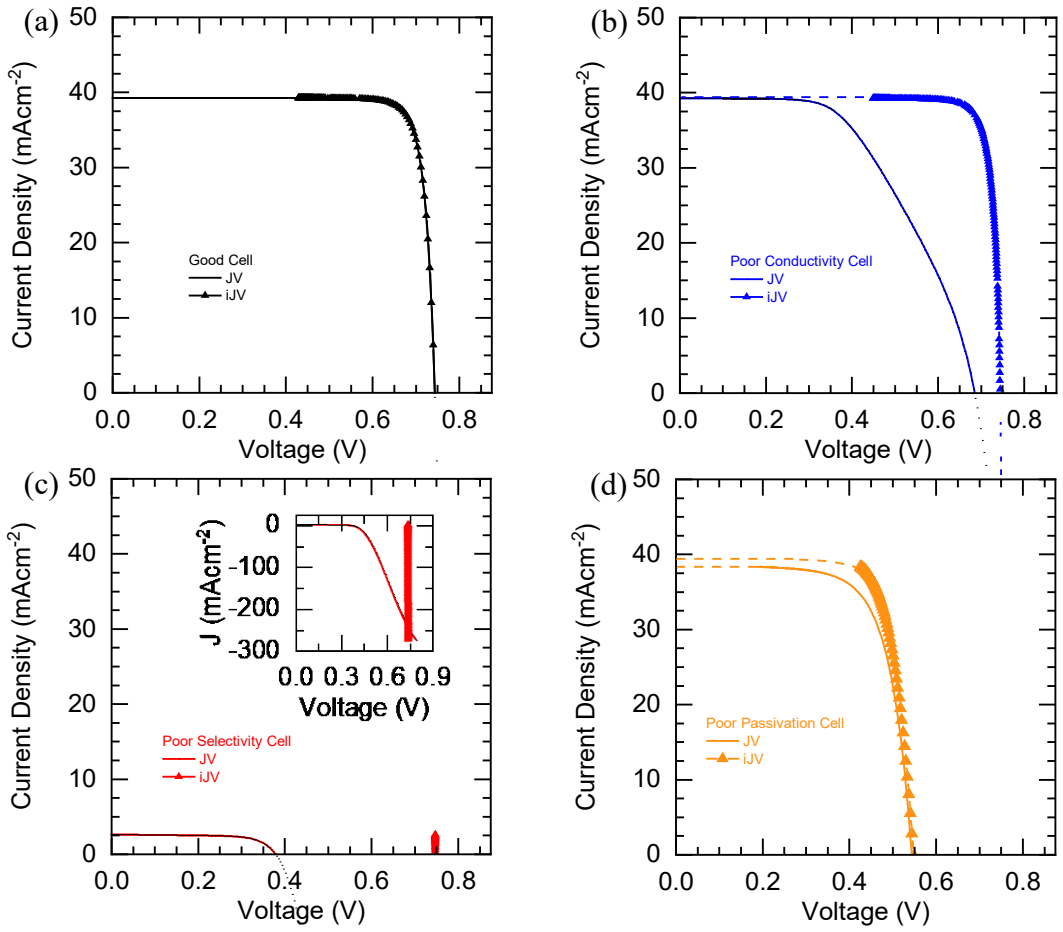

Fig. 8 JV and iJV plots for the four chosen cells. The dashed lines in (b) and (d) are based on pseudo current and reflect what would be observed in an iV measurement as a function of illumination sweep from photoconductance measurements.

The JV curves for the four cells are shown in Fig. 8. For the good cell, the JV and the iJV curves match fairly well.

In the cell with poor contact conductivity, we see the increased series resistance from the slope of the JV curve past the maximum power point. The iJV curve is mostly unchanged compared to the good cell.

The cell with poor selectivity, again, shows the same iJV curve as the previous two cells, but the true JV curve suffers. As expected, the V_{OC} is much lower due to the low

selectivity. In fact, the selectivity at open circuit of this cell can be calculated as discussed in section 2.2, giving us $S \approx 0.5$. For this specific cell, the selectivity is so low, i.e., the contact is so resistive to electrons, that the entire JV curve is affected. This explains the substantially reduced J_{SC}.

The poor passivation cell, still having good selectivity, has a V_{OC} to iV_{OC} ratio close to 1. However, the iV_{OC} itself is substantially lower than what we see in the good cell. This is because the concentration of minority carriers in the contact is high, thus promoting recombination. This also leads to early collapse of the quasi Fermi levels in the absorber, resulting in a low iV_{OC} and, therefore, V_{OC}. Moreover, the J_{SC} is also lower than the good cell, owing to the lower overall conductivity of the contact at a low injection level.

2.7 Equivalence of Partial Specific Contact Resistances to JV

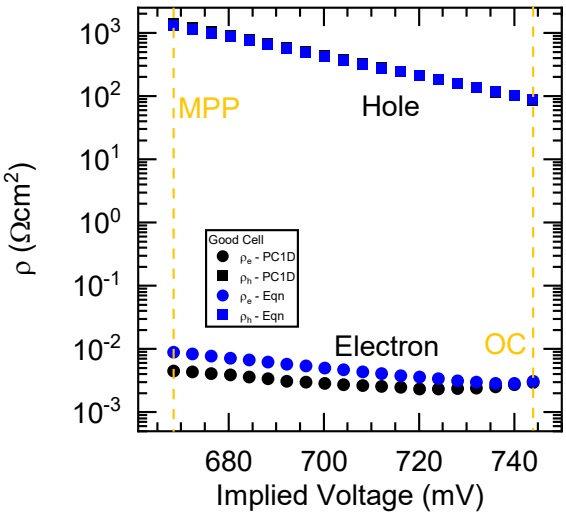

Fig. 9 Resistances vs. implied voltage plot for the good cell.

The goal of this work has been to propose and verify the equivalence of the information contained in the calculated partial contact resistances and current-voltage

characteristics of the solar cell. Using equations (19) and (20) from section 2.4, provided the JV and iJV data from simulations, it is possible to calculate the combined (Absorber + Contact) partial resistances for the electron contact. Also, the resistances can be directly calculated from band diagrams as described by equations (7) and (8) in section 2.3. Comparing these numbers will confirm the validity of the model. Fig. 9 shows the comparison of the resistances obtained from the PC1D band diagrams with the resistances calculated from the equations as a function of implied voltage for the good cell.

For the highly selective and well passivating cell, which is herein called the "good" cell, unsurprisingly, the resistance of the contact to holes is five orders of magnitude higher than the resistance to electrons, and the resistance to electrons itself is fairly low. This results in a solar cell with a V_{OC} of 743 mV and a fill factor of 86%.

The resistances calculated using the equations match excellently at open circuit but seem to diverge as more current is driven. The hole resistances match fairly well and show a relatively small error, remaining below 8% even at the maximum power point. The electron resistances, on the other hand, show a consistent half order of magnitude error through MPP. The possible sources of this error will be discussed later in this section.

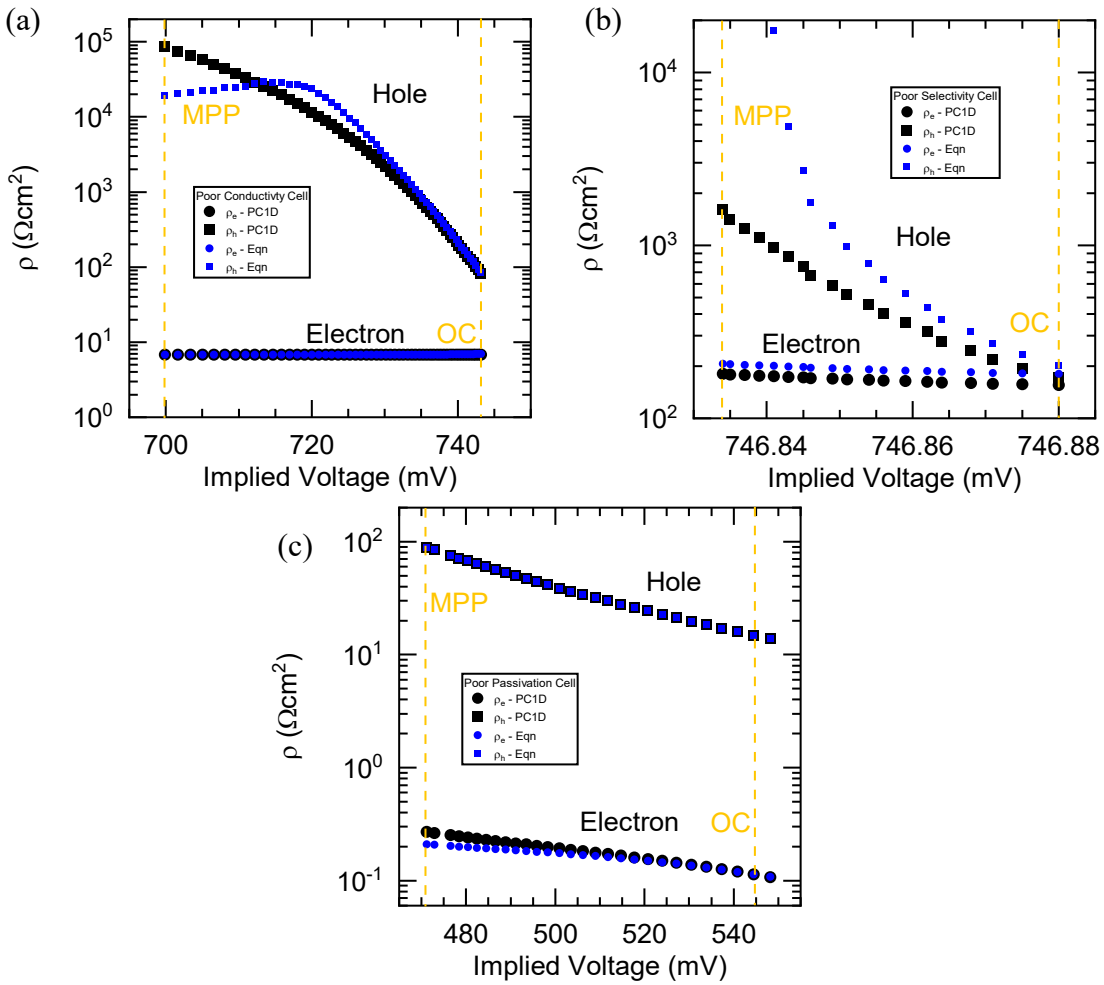

Fig. 10 The three imperfect prototype cells with poorly conductive, poorly selective, and poorly passivating contacts are shown respectively by (a), (b), and (c).

The cell with poor contact conductivity, shown in Fig 10b, still has good selectivity due to low electron mobility while keeping the same hole mobility. In fact, this contact is three orders of magnitude more resistive to electrons than the "good" cell. As observed with the good cell, the resistances match at open circuit and diverge as the device goes towards MPP. Unlike the good cell, the divergence is much more significant for holes but negligible for electrons. This is similar to the poor selectivity contact shown in Fig. 10c. However, in the latter contact, there is an intrinsic error even at open circuit, which may be attributed to a combination of error in precision of input data and quantization limits in

MATLAB's solver. Moreover, the error could be exacerbated by the fact that barely any current is extracted from the device, and there is a significant change in resistance despite almost no change in iV.

The poorly passivating cell (Fig 10c) is more interesting because the behavior resembles the good cell more than the other two prototype cells. The resistance curves, for both electrons and holes, follow a similar trend. It differs from the good cell because the contact is more conductive to holes. Moreover, the error in the calculated resistances for holes match similarly to the good cell, while the electron resistance diverges. Unlike the good cell, however, the error is much lower.

2.8 Contact and Absorber Dominated Resistances

This similarity in the good cell and the cell with poor passivation arises from the fact that the total resistance (Absorber + Contact) for majority carriers on the right side of the cell is dominated by the absorber component in both these cells. This happens because the contacts are highly conductive to electrons, and the bulk resistivity of the absorber itself is more than that of the contact, particularly at low injection, i.e., high current. The poorly passivating cell shows lower iV_{OC} only because it is also more conductive to holes than the good cell, resulting in a leakage of holes from the absorber to the contact, and thus a decrease in quasi Fermi level splitting.

On the other hand, for the other two cells, the resistance to majority carriers is exclusively dominated by the contact. The resistance to electrons is almost constant because the mobility is constant, and the carrier concentration is controlled by the doping

level rather than the injection level. However, the variation in the resistance to holes is entirely driven by the increased depletion of holes in the contact during the flow of current.

2.9 Errors in Calculation

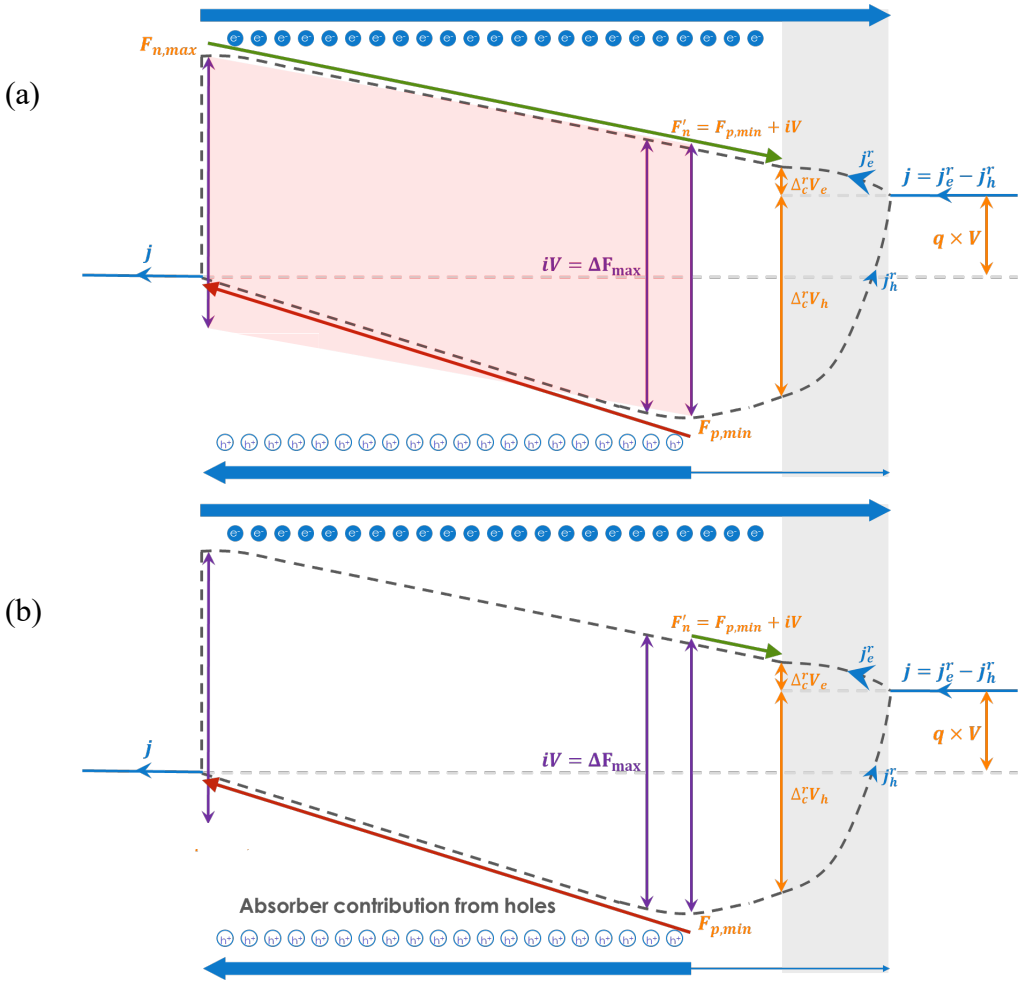

Fig. 11 (a) Original calculation approach. The red area represents part of the absorber, where resistance to electrons is overestimated. (b) Alternative calculation approach.

In the previous section, it was noted that the resistances calculated from the JV and iJV curves do not match perfectly, and the magnitude of mismatch increases with current. The mismatch behavior, however, is different for the absorber dominated and the contact dominated cases. In the absorber dominated cases, the error exists predominantly in the

calculated electron resistance and not in the hole resistance. On the other hand, in the contact dominated cases, there is more error in the hole resistance.

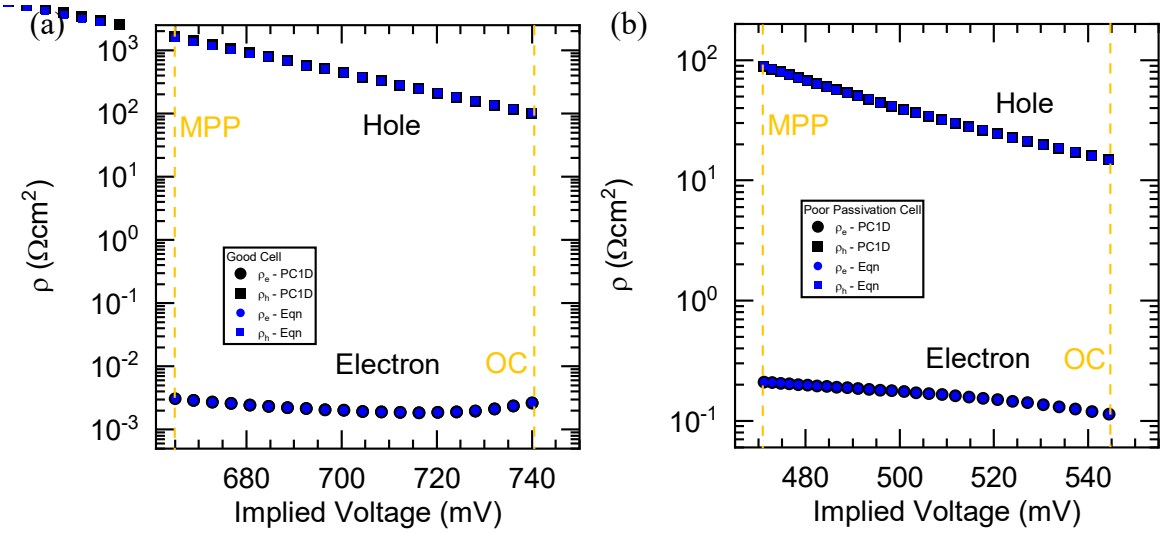

Fig. 12 The two absorber-dominated cases calculated using the reduced contribution of the absorber to the electron resistance.

The error in resistance in the absorber dominated case likely arises from the fact that the approach for calculating the resistance overcounts the contribution in the bulk of the absorber between the inflection points in the quasi Fermi levels as shown in Fig. 11a. In the case being discussed, the inflection point in the electron quasi Fermi level is at the very left of the solar cell due to infinite resistance to electrons in the left contact. When calculating the right-side absorber resistance to electrons, the potential drop is calculated from the maxima of the electron quasi Fermi level, i.e., the left edge of the cell and the absorber contact interface. When current is flowing and, hence, the injection level is low, the concentration of electrons becomes comparable or lower than the p doping of the absorber. This, coupled with the higher electron mobility of silicon, results in an overestimation of the electron absorber resistance, with the overestimation growing with an increase in current (more specifically electron current). A solution to this could be to

only consider the part of the absorber to the right of the hole quasi Fermi level minimum (Fig. 11b). While, admittedly, this would underestimate the absorber contribution to electron resistance slightly, Fig. 13 shows that this effect is not substantial.

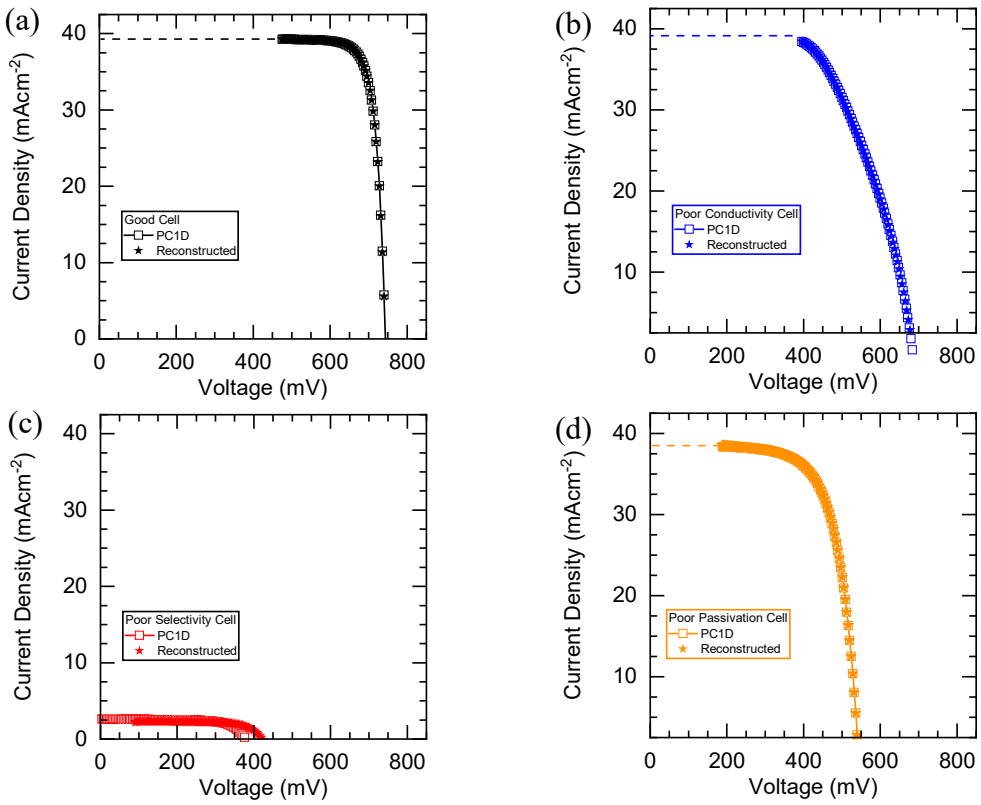

Fig. 13 The JV curves reconstructed using the equations compared to those extracted directly from PC1D.

Despite this approach reducing the error in electron partial resistance in the absorber dominated cases (as shown in Fig. 12), the substantial error in hole resistances for contact dominated cases remain unresolved. However, while the errors exist, they do not affect the device's performance in a meaningful way, as can be seen by reconstructing the JV curves from the resistances obtained from the band diagrams. This is because in the ranges considered, both the contact dominated cells retain their respective properties despite the

error. For instance, the poorly conductive contact remains poorly conductive to electrons despite a substantial mismatch of the hole resistance.

As expected, the JV curves match excellently for the good cell and the cells with the poorly conductive and poorly passivating contact. The cell with poor selectivity does not match well due to intrinsic error in the resolution of the input data, particularly implied voltage.

2.10 Extending to a Larger Set of Solar Cells

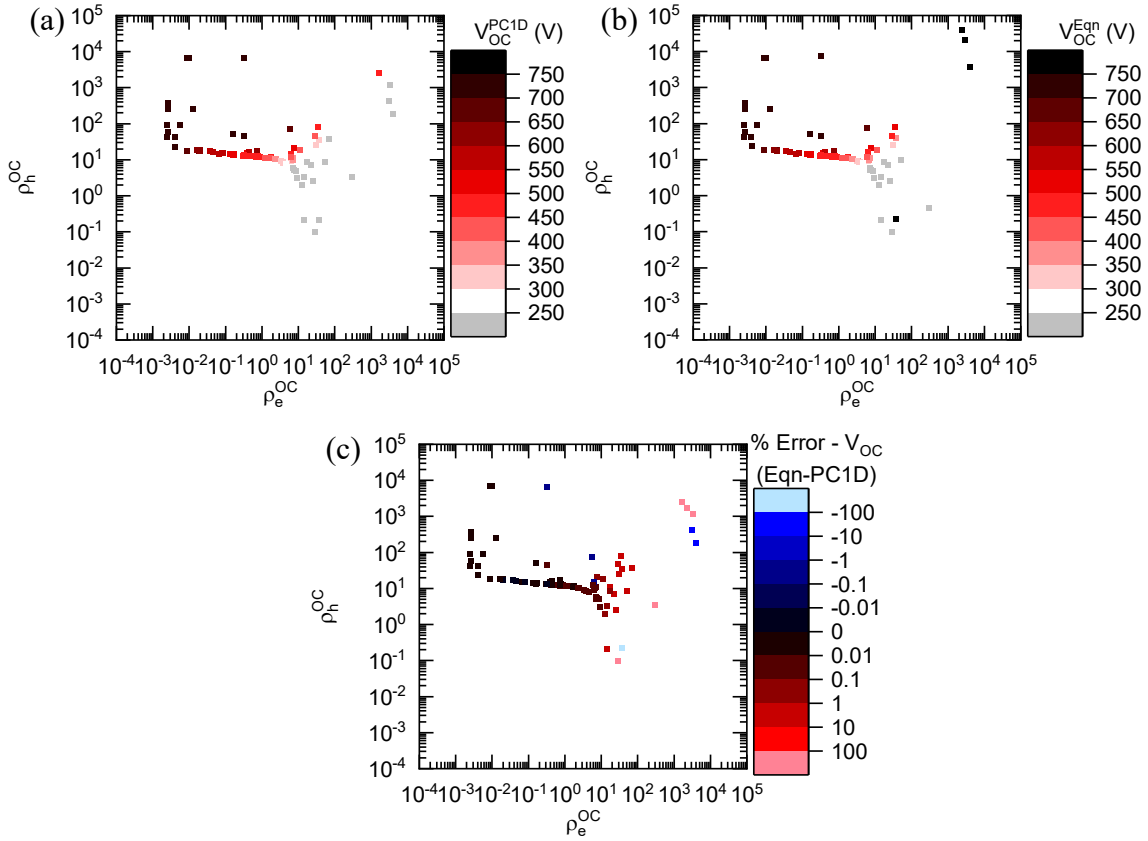

Fig. 14 Colormap of partial resistances at open circuit extracted directly from PC1D (a), and the equations (b). Estimation error is calculated as described in equation (21).

As alluded to in section 2.6, the four prototype cells were drawn from a set of 10400 cells. Ideally, it would be meaningful to reconstruct JV curves from resistances, similarly

to section 2.9, to all 10400 cells. However, this would be practically unviable due to the large computation time required for extracting the JV of a single cell. To circumvent this problem, 100 cells were selected from the pool of 10400, 81 of which were the extremities and medians of the four factors (μ_e, μ_h, N_D, and L_c), and the remaining from a uniform distribution of the 10400 cells. Fig. 15 shows a comparison of the V_{OC} extracted directly from the PC1D JV curves and the reconstructed JV curves. Also shown is the error between the two calculated as defined in equation (21).

$$\%Error = \frac{V_{OC}^{Eqn} - V_{OC}^{PC1D}}{V_{OC}^{PC1D}} \times 100\% \tag{21}$$

Unsurprisingly, the V_{OC} extracted from the reconstructed JV curves match very well with the V_{OC} obtained directly from PC1D. Most of the cells show an error below 0.01%, with a few outliers.

The maximum power point, on the other hand, is more interesting and more relevant because solar cells are meant to operate close to it. Due to the errors in reconstructing the JV curve discussed in section 2.9, the maximum power point itself changes, and as do their corresponding resistances. This means that the data obtained from the equations may not overlap with the data from PC1D. Points that do not overlap are represented with vectors in Fig. 15c and 15f, with the tail at the PC1D MPP and head at the equation MPP. This is done for V_{MPP} and J_{MPP}. Note that percentage errors are calculated similarly to equation (21).

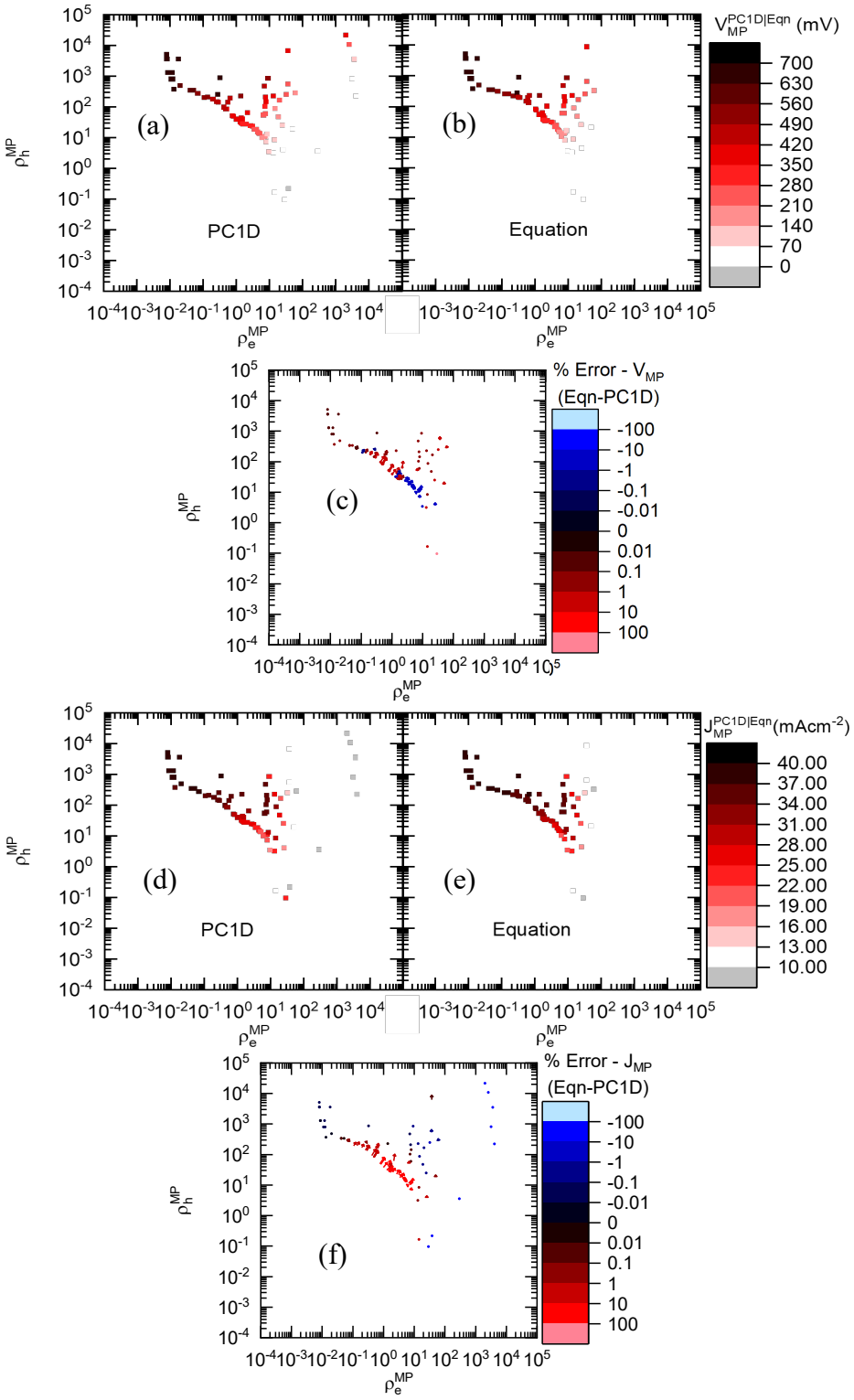

Fig. 15 Color maps of the 100 selected solar cells at maximum power point. (a) V_{MP}^{PC1D}; (b) V_{MP}^{Eqn}; (c) $V_{MP}^{Error\%}$; (d) J_{MP}^{PC1D}; (e) J_{MP}^{Eqn}; (f) $J_{MP}^{Error\%}$

It is evident from the plots that cells with high hole resistance and low electron resistance at the upper left part of the plots show higher V_{OC} and higher J_{SC} while having the least error in either parameter. These cells have highly selective, well passivating contacts. Comparing Fig. 15c and 15f, it is seen that at some points where the equation underestimates V_{MP}, it overestimates J_{MP}. While these cells may not be very relevant due to having poorly selective contacts, it is not easy to interpret the effect on device performance. Looking at errors in fill factor (Fig. 16) may be more relevant in such cases. Moreover, fill factor can also carry information about series resistances, and by extension, contact conductivity.

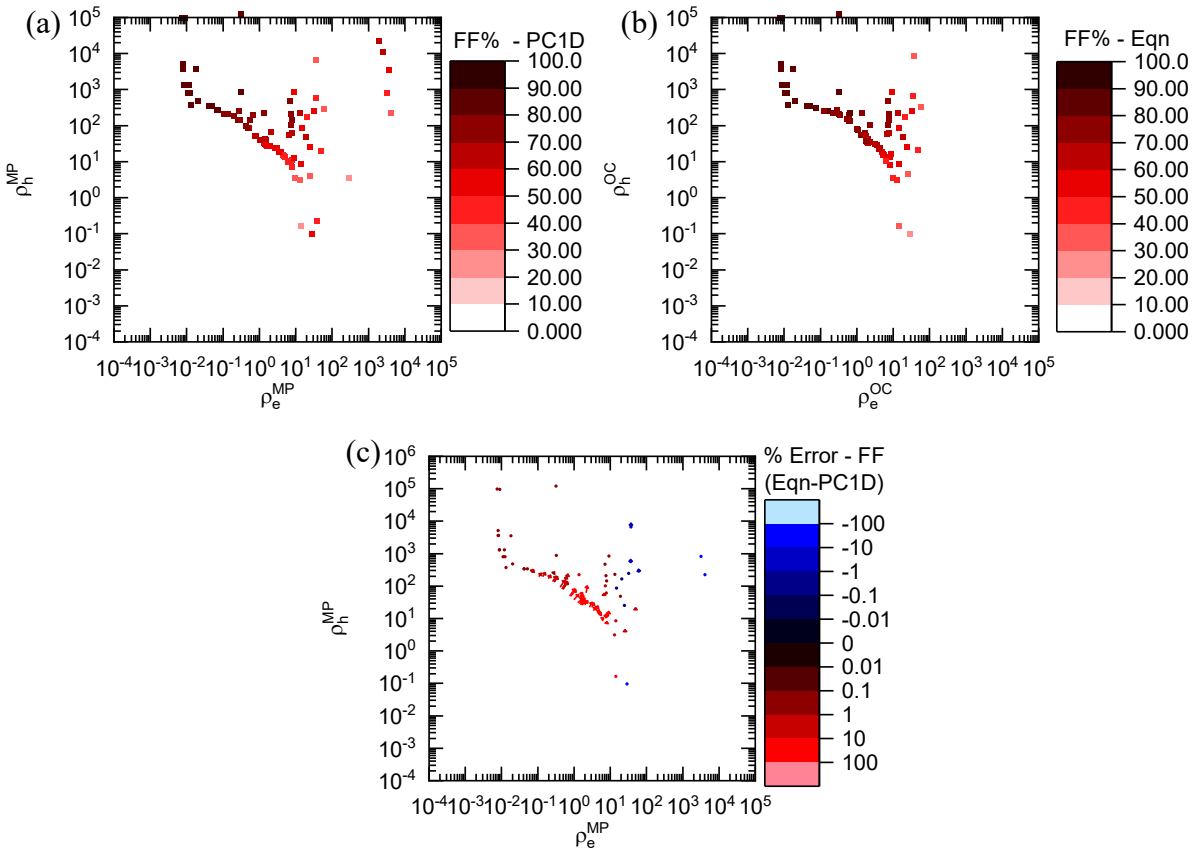

Fig. 16 Fill Factor colormap of partial resistances at maximum power point extracted directly from PC1D (a), and the equations (b).

We see that for most cells that are expected to be selective and passivating (upper left region of the plots), the fill factor is between 70%-80%. As we get further from this region, the fill factor drops sharply. Towards the center of the plot, where the cells have extremely poor selectivity, the error in estimating fill factor is close to 20%. The cells in this region have a J_{MP} below 20 mA cm^{-2}, below half of J_{ph}. Assuming no s-shaped behavior in the JV curves, it can be said that the short circuit current is approximately similar to J_{MP}. This low current output is similar to what was observed in the poor selectivity prototype cell that was discussed in section 2.7. Thus, it would be reasonable to conclude that the reconstruction of the JV curves, or conversely the estimation of resistances from JV and iJV, fail to be accurate when $J_{SC} << J_{ph}$.

2.11 Between Open Circuit and Maximum Power Point

The previous sections explore the behavior of cells at open circuit and maximum power point. At open circuit, the mathematics are simplified, and contributions of absorber resistances are not significant. On the other hand, understanding behavior at the maximum power point is important because that is where the device is expected to operate. Beyond the maximum power point, the results of this model are both less useful and more erroneous. However, the behavior of the cells between OC and MPP has not been discussed yet.

To investigate behavior at intermediate operating points of the device, the resistances at OC and MPP are plotted, and these points are connected by the resistances at every operating point between OC and MPP. Since this is difficult to show for all 100 cells, Fig.

17 focuses exclusively on the four prototype cells. The iV of the cells are conveyed by the color scale.

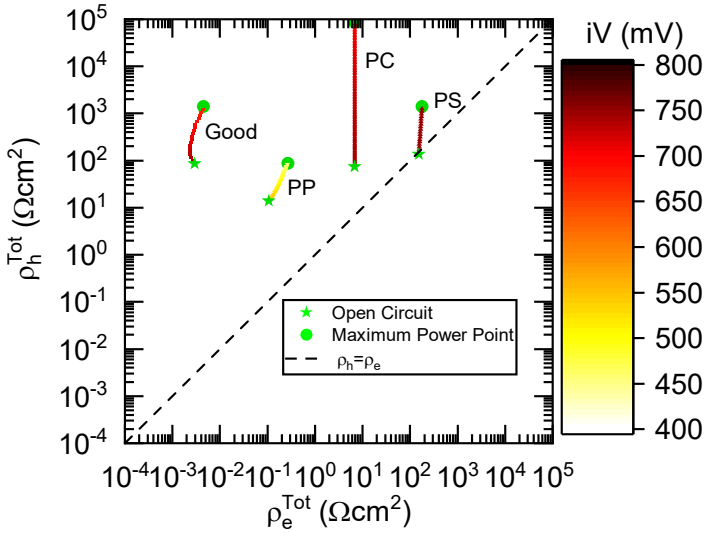

Fig. 17 Plot connecting Open circuit and maximum power point resistances for the four prototype cells. PP=Poor Passivation; PC=Poor Conductivity; PS=Poor Selectivity

The dashed line above marks points where the electron and hole resistances of the contact are the same. If the resistances of a contact lie on this line, then it will necessarily have poor selectivity. This is seen for the poorly selective prototype cell. An electron selective contact will lie above this dashed line, while a hole contact will lie below it. From a plot like this, it is easy to distinguish absorber and contact dominated cells from the orientation of the trail-plot. In this case, the two contact-dominated cells look like straight lines oriented almost parallel to the y-axis, indicating invariant electron resistance. Moreover, the iV of the poor selectivity cell does not change significantly between OC and MPP, indicated by the relatively uniform color.

2.12 Conclusions and Future Directions

The goal of this chapter was to build on the work of Onno et al.[18] by extending the partial specific contact resistance framework beyond open circuit. In doing so, a model of a solar cell was built to understand the behavior of the solar cell when current is flowing in the device and compute the magnitudes of these resistances for contacts. Utilizing this model, I have shown that it is indeed possible to calculate the resistances to a reasonable accuracy when the resistances of the other contact are known or assumed. This model, however, is not very accurate when the current drawn from the cell is extremely low. In such cases, the quasi Fermi level splitting in the absorber changes minimally. As a result, the accuracy of the calculated resistances is determined by the precision or resolution measurement of iV. Regardless, it is unlikely that novel contact materials being developed today are expected to be as poorly selective as the example in this chapter. In essence, it was established that the relationship between the partial specific contact resistances of electrons and holes contain equivalent information to J-V and J-iV characteristics of the solar cell, and the parameters of one system can be calculated from the other system.

It is important to note, however, that the SRV at the contact metal interface was assumed to be 10^{20} cm s^{-1}, which is greater than the speed of light and hence impossible. This was done to treat this parameter like an infinity in PC1D's internal calculations. Despite this, using a more realistic SRV like 10^{7} cm s^{-1} leads to identical results.

Operating within the limits of the model, it is possible to experimentally determine the partial specific resistances of a contact relative to a known reference contact. This can be

demonstrated reasonably well with a silicon heterojunction cell with amorphous silicon contacts.

In this experiment, the i/n aSi:H contact can be treated as a reference, and the i/p hole contact, the test case. To utilize equations (19) and (20), the electron and hole resistances for the i/n contact need to be known. Making a symmetric structure with this contact can be useful for this. Extracting iV from a QSSPC measurement of this symmetric structure will give us $\rho_h^{i/n} + \rho_e^{i/n}$, using equations (19) and (20). Further, $\rho_e^{i/n}$ can be calculated from TLM measurements. One assumption being made here is that the $\rho_e^{i/n}$ is constant, which, as discussed in section 2.7, is not egregiously inaccurate. This process flow is represented by wafer 2 in Fig. 18.

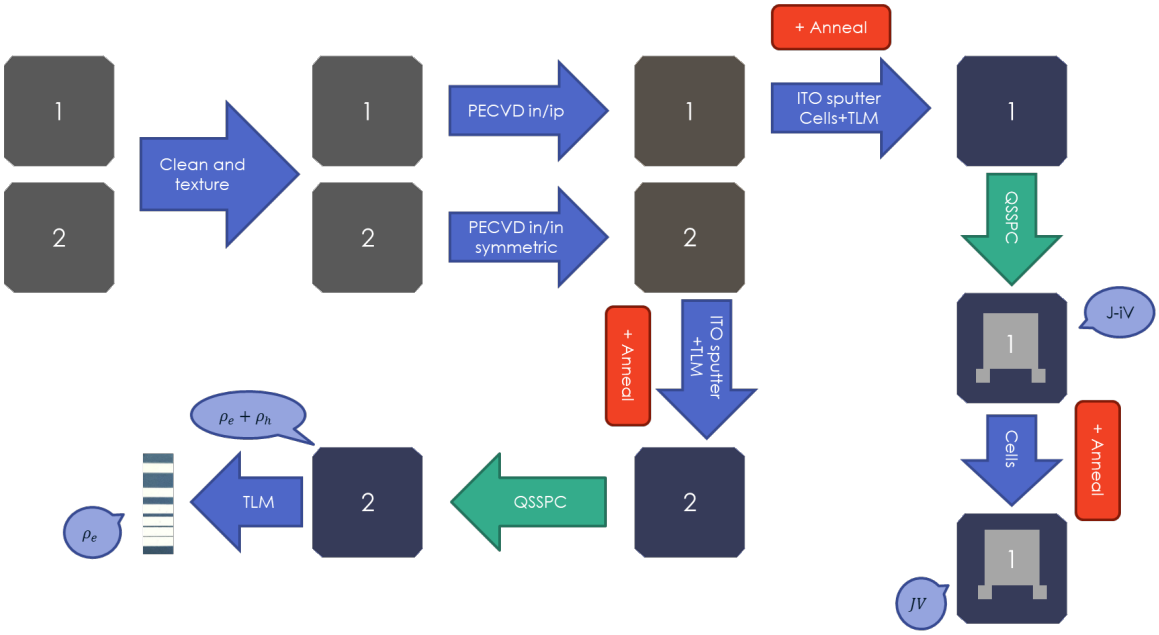

Fig. 18 Proposed process flow for experimental validation of the model and for extracting contact resistances for novel contacts.

Once the reference contact is known, full cells can be fabricated and tested. It is important to note, however, that since this model does not account for recombination at the

absorber contact interface, the wafers need to have excellent surface passivation, ideally an iV_{OC} above 730 mV.

In the analysis in section 2.7, the absorber's contribution to the majority carrier resistance of the reference contact was used as an input for the model. This cannot be practically measured and must be assumed to be zero. For a contact that is extremely conductive to majority carriers, which in this experiment are holes, the absorber's contribution will be significant. Therefore, it is important to have an absorber with bulk resistivity as low as reasonably possible and a reference contact that is at least ten times more resistive than the absorber. Using a standard CZ wafer with doping of $1.5 \times 10^{15}\ \mathrm{cm}^{-3}$, the bulk resistivity when quasi Fermi level splitting is minimum is approximately $30\ \mathrm{m\Omega\ cm}^{-2}$. This means that the i/n contact will need to have a contact resistivity close to $300\ \mathrm{m\Omega\ cm}^{-2}$ which is not practically unreasonable. Once the cell is fabricated, the JV curves can be obtained from standard sun simulator measurements and the iJV curve from ERE measurements where the voltage is varied.

While this experiment is proposed for amorphous silicon-based contacts, virtually the same process will work for any novel, unknown contact for a solar cell with a known reference.

CHAPTER 3

SIMULATION OF SILICON HETEROJUNCTION CELLS IN AFORS-HET

3.1 Introduction

The previous chapter aimed at building a fundamental device model of a solar cell that can be used to analyze contacts based on a known reference. This is useful in validating the viability of a novel contact material for use in a device and in diagnosing the poor performance of contacts. Such a simplified model, however, is insufficient in predicting the effects of specific material or device structure changes on the performance of a complete solar cell.

Higher-level numeric simulation programs are required to understand which layers in a device stack are affecting performance or if there are specific material properties to target to avoid performance bottlenecks. This can be achieved using either finite element or finite difference simulation approaches.

Finite element simulations involve solving fundamental semiconductor equations in a geometrically small piece (element) of the semiconductor, based on pre-defined boundary conditions, and then using the results for that piece as a boundary condition for the next element. Cumulating the performance of all the pieces will reflect the performance of the complete device. PC1D, used in the previous chapter, is an example of such a program[42].

On the other hand, finite difference simulations are performed by, again, dividing the layers of the solar cell into finite elements but solving the semiconductor equations at the edges/boundaries (points in a 1D case) of these elements[44]. The points are called grid points. The material properties of the layers are defined for each grid point, and electric

field, carrier density, current, and other electrical parameters are evaluated at each of these points. The accuracy of this kind of method is dependent on the layout of these grid points. For instance, thin layers and regions near interfaces require denser grids, while a sparser grid is sufficient in the bulk of semiconductors for accurate results.

In this chapter, AFORS-HET v2.5 (automat for simulation of hetero-structures)[23], a 1D numerical finite difference simulation program, is used. The goal of this chapter is to simulate silicon heterojunction solar cells with aSi:H contacts[45] to a degree of accuracy consistent with experimental results. This will allow for a drop-in replacement of one or both of the contacts with novel materials to predict potential performance improvements or deterioration.

3.2 Transport in Silicon Heterojunction Solar Cells

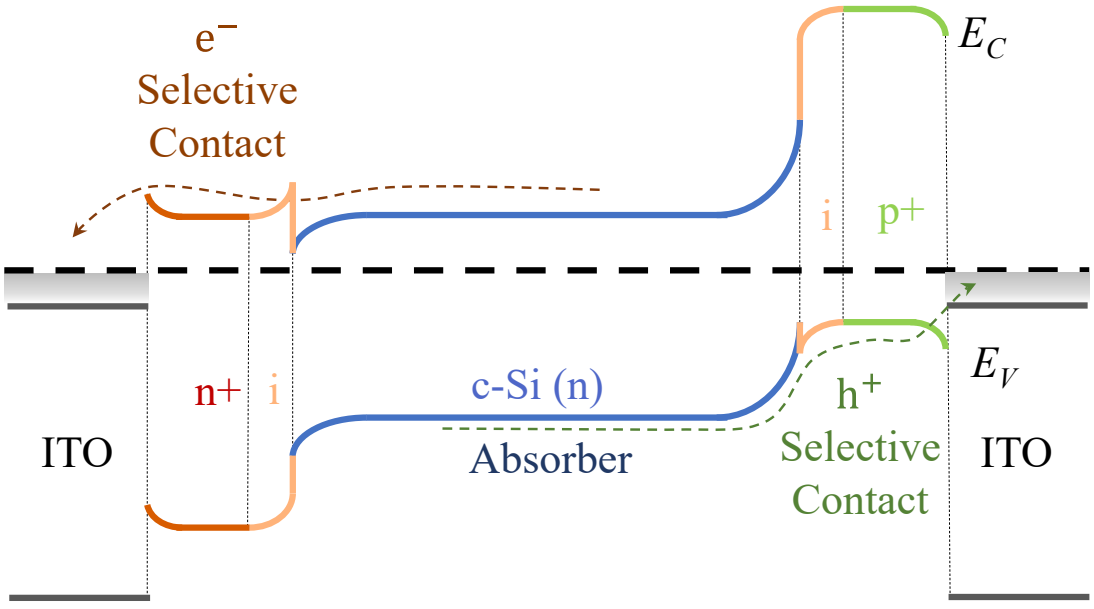

Fig. 19 Schematic band diagram of an SHJ cell indicating charge carrier transport.

Fig. 19 shows a schematic band diagram of a silicon heterojunction cell like the one investigated in this chapter and will serve as a reference for this section. Silicon heterojunction cells photogenerate carriers in a doped crystalline silicon wafer. This wafer is flanked by thin intrinsic hydrogenated amorphous silicon layers that chemically passivate the dangling bonds on the absorber contact interface, thereby reducing defect density and preventing recombination[46]. These amorphous silicon layers need to be thin due to their low carrier concentration and mobility, which can affect the series resistance[47]. Beyond the passivation layer, an additional layer of doped amorphous silicon is deposited to perform as the carrier selective contact. These carrier selective contacts impart the necessary band bending for effective carrier separation. Although these doped layers can provide some field-effect passivation, intrinsic amorphous silicon provides significantly better chemical passivation to the absorber interface, making it insufficient to only use these doped layers on the silicon absorber[48,49]. These amorphous silicon layers are typically deposited by PECVD.

The bandgap of amorphous silicon is 1.72 eV, which is higher than crystalline silicon's 1.12 eV. This results in band offsets at the absorber contact interfaces, as shown in Fig. 19. Therefore, the right doping in the aSi:H contact layers is important. An insufficiently doped contact will not just affect selectivity but will also result in a high Schottky barrier for the majority carriers of the contact. While it is true that this barrier typically exists in all SHJ cells, it is usually low enough to be overcome by thermionic emission or tunneling. A more heavily doped contact will generate a thinner depletion region and increase the tunneling current[22].

To drive a circuit using the extracted carriers collected by the contacts, good metallization is important. For most solar cells, carriers are extracted from the front through a metallic grid and by a continuous-coverage metal layer at the back. For SHJ solar cells, this is typically insufficient due to poor lateral conductivity of the aSi:H layers[50]. This problem can be circumvented through the use of a wide-bandgap transparent conductive oxide like ITO coated on the amorphous silicon. This performs both as a lateral transport layer and as an optical coating (anti-reflection on the front and reflection enhancer on the back) in SHJ devices[8].

The work function of the ITO layers is also important to ensure appropriate band alignment and can be easily adjusted over a wide range through doping[51]. Too low a work function can deplete the electron contact to the point of blocking majority carriers. However, for typical work functions around 4.5 eV and below, the electron contact is both selective and ohmic.

On the other hand, the p-aSi:H/ITO junction is more interesting. For typical doping levels in the p contact and typical ITO work functions, the Schottky barrier for hole transport is too high, which should theoretically result in high contact resistances and s-shaped JV curves[52,53]. This can be ameliorated through higher doping of the p-layer, but it has been observed that increased boron doping can cause hydrogen effusion from the intrinsic layer, thereby deteriorating passivation[54]. Experimental contact resistance measurements suggest that a band to band tunneling based mechanism must be active at low work functions of ITO[47]. This trap-assisted tunneling inter-band mechanism has been suggested to be a significant contributor to realistic device performance[55].

3.3 The AFORS-HET Simulation Program

As stated above, the AFORS-HET program performs 1D numerical electrical simulations for a device based on defined device structure and material properties. It is also possible to define characteristics of the interfaces between layers, including tunneling through thin insulators.

Once the device is defined, it is essential to design a grid layout optimal to the device being simulated. Incorrect grid layout, primarily from insufficient grid point density, can lead to inaccurate results or non-convergence of the simulation. On the other hand, having too high a grid point density can slow down computation substantially. It is common to, therefore, use a higher density of grid points near the interfaces and logarithmically decrease the grid point density towards the bulk of the semiconductor layers. This gradient in grid point density, however, does not matter in extremely thin semiconductors. In fact, grid points too close to a tunneling interface can often cause failure of convergence.

There are some key limitations to AFORS-HET. Primarily, all density of state calculations are performed using the Boltzmann approximation of the Fermi-Dirac function[56]. This works quite well for lightly doped semiconductors but is inaccurate for heavily or degenerately doped ones, particularly those used in contacts or TCOs[55,57]. However, this issue can be worked around by carefully initializing the simulation (with potentially unrealistic inputs) to yield realistic results. This makes it difficult to accurately use experimentally derived dopant densities for the contact layers, but the simulation remains useful for comparative studies.

The other significant limitation of the current version of AFORS-HET is the inaccuracy of the optical model. While AFORS-HET is not designed to be used as a reference for the optical properties of a device, its optical model is necessary for accurately calculating photogeneration, the short circuit current, and efficiency. There are two optical models in use in AFORS-HET. The first is based on Beer-Lambert law, and the program calculates the absorptions in each layer over one or many passes.

The second model utilizes multiple reflections and scattering at the interfaces. This model is expected to be more accurate and can account for optical effects at textured surfaces. To use this model, the refractive index and extinction coefficient as a function of wavelength are used as inputs. Still, this model tends to overestimate reflections into the atmosphere from the front surface. This causes an underestimation of the short circuit current. However, it can be worked around by increasing the illumination intensity to match experimental J_{SC} numbers. Of these two models, the former will be used in this chapter.

3.4 Simulation Details

A device structure similar to that used by Leilaeioun et al. was simulated[47] here. This stack is shown in Fig. 20, and the material properties used are noted in table 3.

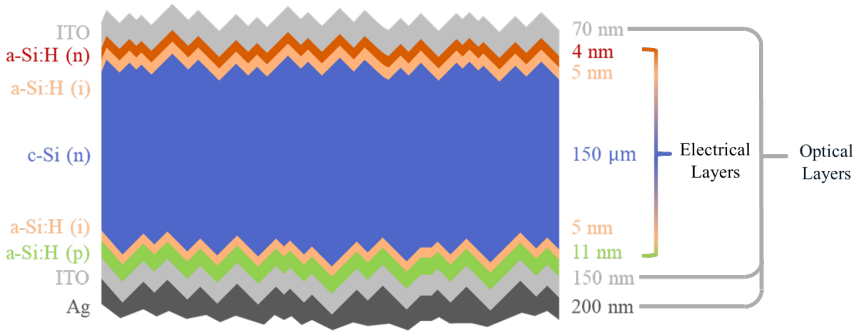

Fig. 20 Schematic of the silicon heterojunction cell used in the simulations. In AFORS-HET, degenerate semiconductors and metals need to be treated as optical layers. Therefore, the stack of electrical layers starts from the aSi:H (n) and ends at aSi:H (p).

Table 3 Material parameters of the layers used in the SHJ cell. These parameters are obtained from AFORS-HET's internal layer files.

	Electrical Layers			
Layer / Parameter	c-Si (n)	a-Si (i)	a-Si (n)	aSi (p)
Thickness (nm)	1.5×10^5	5	4	11
Dielectric Constant (κ)	11.9	11.9	11.9	11.9
Electron Affinity ($\chi; eV$)	4.05	3.9	3.9	3.9
Bandgap ($E_g; eV$)	1.124	1.72	1.72	1.72
Effective Conduction Band DOS ($N_C; cm^{-3}$)	2.846×10^{19}	1×10^{20}	1×10^{20}	1×10^{20}
Effective Valence Band DOS ($N_V; cm^{-3}$)	2.685×10^{19}	1×10^{20}	1×10^{20}	1×10^{20}
Electron Mobility ($\mu_e; cm^2V^{-1}s^{-1}$)	1111	20	20	20
Hole Mobility ($\mu_h; cm^2V^{-1}s^{-1}$)	421.6	5	5	5
Acceptor Doping ($N_A; cm^{-3}$)	0	0	0	7.47×10^{19}
Donor Doping ($N_D; cm^{-3}$)	1.5×10^{16}	1000	7.084×10^{19}	0
Electron Thermal Velocity ($v_e; cm\ s^{-1}$)	10^7	10^6	10^6	10^6
Hole Thermal Velocity ($v_h; cm\ s^{-1}$)	10^7	10^6	10^7	10^7
Auger Electron Recombination Coefficient ($cm^6\ s^{-1}$)	2.2×10^{-31}	0	0	0
Auger Hole Recombination Coefficient ($cm^6\ s^{-1}$)	9.9×10^{-32}	0	0	0

The defects states used for the amorphous Silicon layers were derived from AFORS-HET's library. The metal-semiconductor interfaces were set to have surface recombination velocities for both electrons and holes equal to 10^7 cm s^{-1}, and had tunneling enabled for Schottky barriers[58].

The Auger recombination coefficients in this simulation were set as constants as defined in table 3. Utilizing injection dependent Auger recombination coefficients suggested by Richter et. al.[59] will result in lower open circuit voltages, but the constant recombination coefficients are sufficient for comparative studies.

As suggested in section 3.2, trap-assisted tunneling is essential for accurate simulation of the rear p-aSi:H/ITO junction. However, AFORS-HET's TAT implementation, derived from the theory of Hurkx et al., is inconsistent and prone to crashing and hence, could not be utilized in this simulation. Moreover, implementing TAT involved treating the ITO as a degenerate wide bandgap semiconductor layer, which is inaccurate in AFORS-HET due to the use of Boltzmann statistics. To circumvent this, the ITO layers were treated as a metal of constant work function for simulation. The work functions of both layers were set to flat-band potentials, resulting in a work function of 4.2 eV at the front and 5.1 eV at the rear, neither of which are outside the range of realistic ITO work functions[51].

As discussed before, AFORS-HET models the optical behavior of the device in one of two ways, either through a multiple reflections and coherence model or using Beer-Lambert law. While the former is expected to be more accurate, it tends to overestimate reflections in the near UV range. Therefore, in this work, the Beer-lambert law optical model was used. For accurate estimation of photogeneration, the path length factor was set

to 50, which is considered realistic for current light trapping measures for SHJ cells[60]. Furthermore, this device structure was simulated in Sunsolve[61] to obtain front surface reflection and absorption in the front ITO, which were used as inputs for AFORS-HET. Fig. 21 shows a comparison of the fraction of light absorbed in the crystalline silicon, as obtained from AFORS-HET's model and SunSolve, as a function of wavelength. We see that AFORS-HET's model matches the ray-traced SunSolve model's prediction fairly well in most wavelengths but overestimates the absorption in the near-IR range slightly. The source of this small error is not investigated in this chapter.

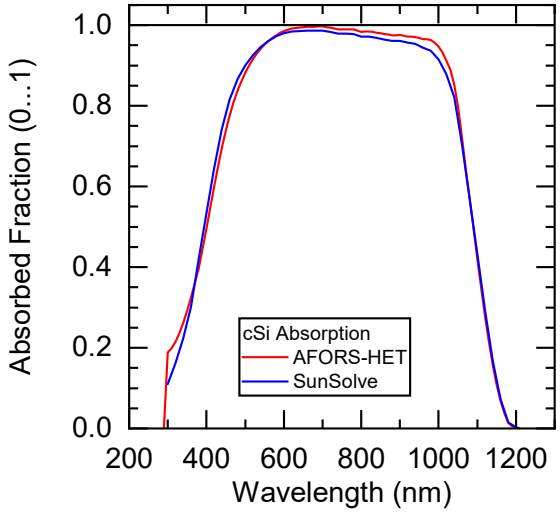

Fig. 21 A comparison of the fraction of light absorbed in the crystalline silicon layer as computed by AFORS-HET and SunSolve.

3.5 Simulated Cell Results

Fig. 22 shows the results of the device simulated based on the setup described in section 3.4 overlayed by the JV characteristic of an experimental device based on the same structure. It is seen that the open circuit voltages for the simulated and experimental cells are very similar and within experimental error. This suggests that the passivation and selectivity are well simulated in the model through defect states and doping in the aSi:H

layers and TCO work function. The simulated cell, however, does have a higher series resistance. This likely arises from the fact that trap-assisted tunneling was not implemented, which would aid hole transport at the rear contact. This reflects in the higher fill factor of the experimental cell. However, a lower short circuit current was observed for the experimental cell. This is likely due to increased parasitic absorption in the experimental cells, and it is not uncommon for cells based on this structure and similar processing[62] to have J_{SC} exceeding 40 mA cm^{-2}.

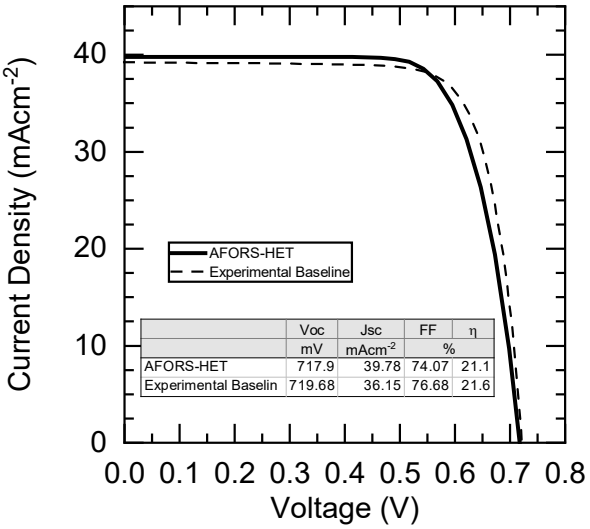

Fig. 22 A comparison of the ASORS-HET simulated JV curve with that of an experimental solar cell of the same structure. Experimental data courtesy of David Quispe of Arizona State University.

3.6 Application to Novel Contacts: AlGaAs

The goal for developing a realistic model of an SHJ cell is to allow for understanding potential performance gains or losses from making changes to the device structure. One of the most significant loss mechanisms impeding performance is parasitic absorption from the amorphous silicon layers[8]. This has motivated the use of new wide bandgap materials with good selectivity as attempts to enhance the optical performance of the SHJ device structure[11,12].

III-V semiconductors are widely known to be materials of highly tunable optoelectronic properties, particularly bandgap[63]. It is also possible to grow polycrystalline III-V layers with high doping and thus high conductivity[64]. Moreover, many of these materials can be deposited using common plasma processes like sputtering, reducing the need for additional tooling for the growth of these layers for non-epitaxial applications[65–69]. This suggests the viability of amorphous or polycrystalline III-V semiconductors as a potentially inexpensive replacement for existing silicon heterojunction based solar cell structures.

Table 4 AFORS-HET electrical input parameters used for $Al_{0.8}Ga_{0.2}As$

Parameter \ Layer	$Al_{0.8}Ga_{0.2}As$ (p)
Thickness (nm)	11
Dielectric Constant (κ)	10
Electron Affinity ($\chi; eV$)	3.77
Bandgap ($E_g; eV$)	2.07
Effective Conduction Band DOS ($N_C; cm^{-3}$)	1×10^{20}
Effective Valence Band DOS ($N_V; cm^{-3}$)	1×10^{20}
Electron Mobility ($\mu_e; cm^2V^{-1}s^{-1}$)	20
Hole Mobility ($\mu_h; cm^2V^{-1}s^{-1}$)	5
Acceptor Doping ($N_A; cm^{-3}$)	1×10^{18}
Donor Doping ($N_D; cm^{-3}$)	0
Electron Thermal Velocity ($v_e; cm\ s^{-1}$)	10^7
Hole Thermal Velocity ($v_h; cm\ s^{-1}$)	10^7
Auger Electron Recombination Coefficient ($cm^6\ s^{-1}$)	1×10^{-31}
Auger Hole Recombination Coefficient ($cm^6\ s^{-1}$)	1×10^{-32}

In this section, p-$Al_{0.8}Ga_{0.2}As$ will be investigated as a prototype III-V semiconductor contact. Since this study focuses primarily on the electrical properties of this contact, the p-$Al_{0.8}Ga_{0.2}As$ was used as a replacement for the rear amorphous silicon layer, and its optical properties were set to $n = 4$ and $k = 0$. Table 4 contains the input material properties for this layer in AFORS-HET. It is important to note that the material simulated was a perfect crystal with no defect states.

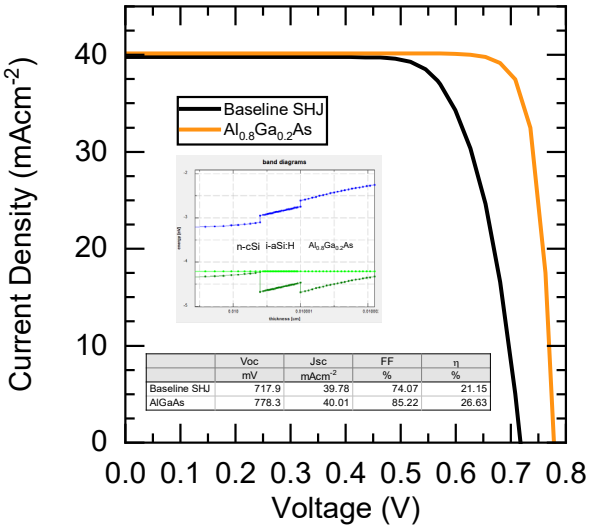

Fig. 23 The JV curve of the AlGaAs contact cell compared to the SHJ simulation discussed in section 2.5. The inset shows the band diagram of the contact/absorber interface.

The results of this simulation are shown in Fig. 23. The cell seems to have a substantially higher V_{OC} than the baseline SHJ cell, but this gain cannot be practically observed because the simulated AlGaAs layer was defect-free, resulting in unrealistically efficient carrier transport through the contact. Moreover, a silicon solar cell of the thickness used in the simulations with ideal contacts and perfect passivation is limited to a V_{OC} of around 760 mV due to Auger recombination[70]. It is likely that the increase in V_{OC} is exacerbated by the use of the constant Auger recombination coefficient as described in section 3.4. In fact, using more accurate recombination coefficients does result in a lower V_{OC}, but the results will be difficult to compare to those shown in section 3.5. However, a smaller V_{OC} gain may not be impossible to achieve, depending on the doping of the AlGaAs layer. The fill factor has increased because of the same reason. The J_{SC}, on the other hand, is practically identical due to relatively similar optical behavior in this simulation arising from using this layer as a replacement for the back contact.

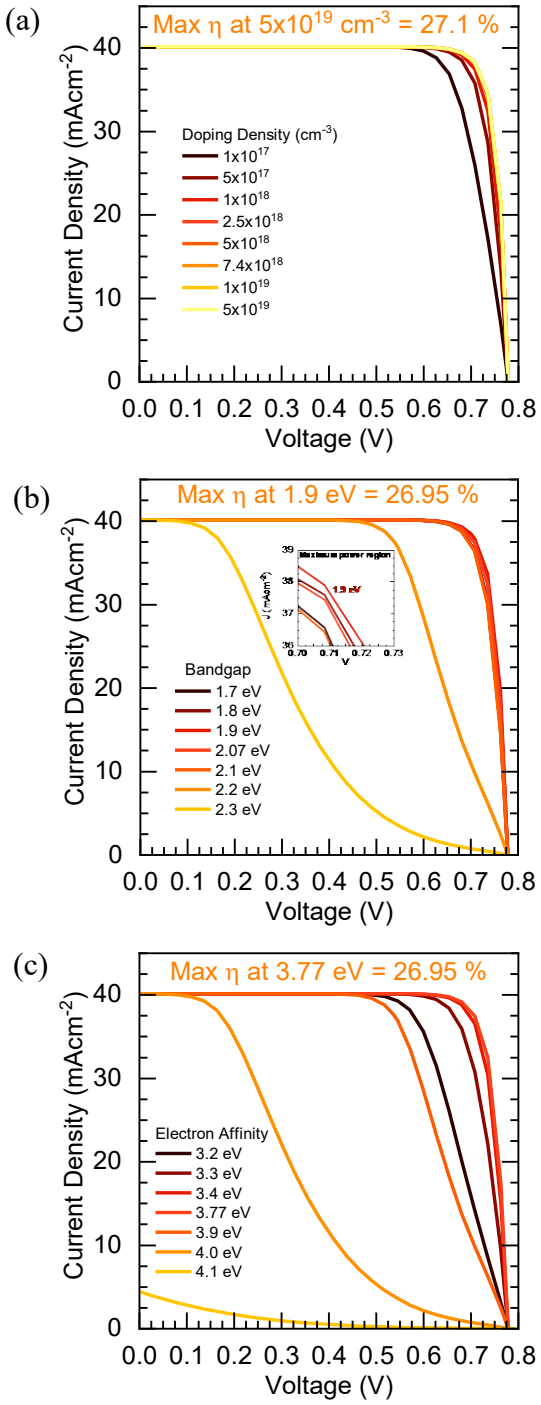

Fig. 24 Effects of material parameter variation in the AlGaAs layer. (a) Doping; (b) Bandgap (Inset shows the MPP region of the curves in detail); (c) Electron Affinity

Changing the doping in the AlGaAs layer affects the selectivity of the contact. Unsurprisingly, increasing the doping in this layer consistently increases the efficiency of the resultant device. However, as the doping density approaches degeneracy, the benefits of increased doping start diminishing. This behavior is seen in Fig. 24a. Moreover, very high fractions of dopant atoms can, in practical cells, result in a poorly passivating contact. Therefore, it is likely that there is an upper limit to efficiency gains from increasing doping.

One of the advantages of using a III-V semiconductor is the relative ease of tuning the bandgap through changing the stoichiometry of the ternary compound. Fig. 24b shows the effect of variation of the bandgap has on the performance of the device. We see in the high bandgap cases that the JV curves become increasingly s-shaped. This arises because increasing the bandgap without commensurately increasing the doping results in a higher Schottky barrier for holes at the i-aSi:H/AlGaAs hetero-interface. The cells with AlGaAs bandgaps below 2.2 eV have very similar efficiencies and fill factors.

Changing the electron affinity will adjust the position of the conduction band edge relative to the rest of the device. From Fig. 24c, we see that an optimal electron affinity exists. When the electron affinity is too low, the i-aSi:H is more deplete of holes than both the contact and the absorber's edge. This likely results in increased contact resistance at this interface. On the other hand, when the electron affinity of the contact layer exceeds the electron affinity of the aSi:H layer, it will cause the hole contact to block the backflow of electrons when the circuit is completed, causing a decrease in current.

3.7 Conclusions

In this chapter, an SHJ cell in AFORS-HET consistent with experiments was simulated. This model can be used for drop-in replacements of layers or device structure changes to test effects on solar cell performance. Here, AlGaAs was discussed as an example, but any material with known properties can be used. It was observed that changing the band alignment through electron affinity, doping (work function), and bandgap can affect the selectivity of the contact as well as contact resistance due to changes in the height of the Schottky barrier. It was observed that doping has a lesser effect on the fill factor than the other two parameters over the ranges the parameters were varied. The dependance of device performance metrics on these material parameters can be quantified by plotting the variation of the device metric with percentage changes in material properties. This kind of sensitivity analysis of performance can be represented as a tornado plot to determine the most significant material parameters for solar cell performance. For future work, it would also be useful to simulate replacement front contacts with potential benefits to the optical properties of the solar cell. This kind of simulation can also be attempted by reversing the stack of the cell.

CHAPTER 4

SIMULATION OF TOPCON-LIKE CELLS IN AFORS-HET

4.1 Introduction

While SHJ cells like those discussed in *chapter 3* are currently the champions of efficiency for non-concentrated silicon photovoltaics due to their exceptional electrical properties, their fabrication is more difficult than currently popular solar cell technologies. The amorphous silicon used in SHJ cells effuse hydrogen above 300°C, thereby damaging passivation[71,72]. These temperature restrictions and more difficult process control make it difficult for current diffused junction and PERC/PERL production lines to transition to fabricating SHJ cells without investing in expensive tooling.

Feldmann et al. in 2013 proposed the use of a tunneling oxide layer capped by doped polycrystalline silicon at the rear of the solar cell with a passivated diffused junction front, reaching an initial efficiency of 23.7%[73]. This kind of device stack has many of the benefits of selective contacts while still being compatible with high temperature processing techniques. Feldmann et al. called this kind of device a *tunnel-oxide passivated contact* (TOPCon) solar cell. An improvement to this design would be to use doped polycrystalline silicon contacts with oxide passivation on both sides of the solar cell[74]. This will allow for lower recombination at the front of the solar cell compared to a diffused junction. This kind of double-side TOPCon device will form the basis of most discussion in this chapter.

The double-side TOPCon device, however, suffers from increased parasitic absorption due to the thick front poly-Si layers. If the poly-Si layer is too thin, the contact is not selective enough for effective carrier collection, leading to low fill factors. Moreover, the

boron doping in the p-type poly-Si contact can diffuse through the oxide into the crystalline silicon absorber at high temperatures. This can result in a buried doped layer negating the benefits of the oxide passivation[25]. These shortcomings of current double-side TOPCon cells motivate the development of a simulation model of such a solar cell to allow for modifications to materials, like those shown in *chapter 3*, or alternate contact materials that may overcome these current limitations.

4.2 Basic Simulation Setup

A double-side oxide passivated cell with polycrystalline silicon contacts was simulated in AFORS-HET v2.5 based on a design similar to that used by Young et. al[75]. This structure has a textured front and a planar rear, with thin tunneling oxide on the n-doped crystalline silicon absorber and heavily doped poly-Si contacts. Note that the lateral conductivity in the poly-Si is high enough that a separate lateral transport layer like a TCO is not needed. Like in the previous chapter, both metal contacts were set to flat band work function. The material parameters used for the electrical layers are shown in table 5. Also, Beer-Lambert law was used with a path length factor of 50. The front surface reflectance was obtained from a raytracing simulation in SunSolve[61] based on the device structure shown in Fig. 25.

The tunneling oxide layers were defined as interfaces between the crystalline silicon and the contacts. They were set to be of a thickness of 1.2 nm with a fixed dielectric constant of 3.9. The bandgap and electron affinity were set to better reflect realistic barrier heights for the tunneling process, as is discussed in later sections. Also, the Wentzel–

Kramers–Brillouin (WKB) approximation for solving linear differential equations was enabled in AFORS-HET to improve simulation speed.

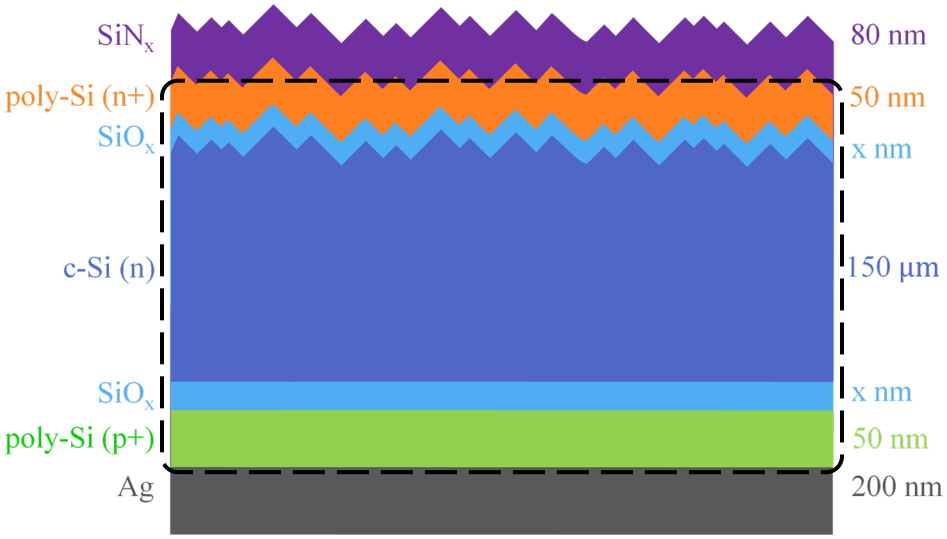

Fig. 25 Schematic of the double-side oxide passivated solar cell with poly-Si contacts. The dashed line bounds the electrical layers.

Table 5 Material properties used in the double-side TOPCon cell

	Electrical Layers		
Parameter \ Layer	c-Si (n)	poly-Si (n)	poly-Si (p)
Thickness (nm)	1.5×10^5	50	50
Dielectric Constant (κ)	11.9	11.9	11.9
Electron Affinity ($\chi; eV$)	4.05	4.05	4.05
Bandgap ($E_g; eV$)	1.124	1.12	1.12
Effective Conduction Band DOS ($N_c; cm^{-3}$)	2.846×10^{19}	1×10^{20}	1×10^{20}
Effective Valence Band DOS ($N_v; cm^{-3}$)	2.685×10^{19}	1×10^{20}	1×10^{20}
Electron Mobility ($\mu_e; cm^2V^{-1}s^{-1}$)	1111	100	20
Hole Mobility ($\mu_h; cm^2V^{-1}s^{-1}$)	421.6	50	5
Acceptor Doping ($N_A; cm^{-3}$)	0	0	9×10^{19}
Donor Doping ($N_D; cm^{-3}$)	1.5×10^{16}	7×10^{19}	0
Electron Thermal Velocity ($v_e; cm\ s^{-1}$)	10^7	10^7	10^7
Hole Thermal Velocity ($v_h; cm\ s^{-1}$)	10^7	10^7	10^7
Auger Electron Recombination Coefficient ($cm^6\ s^{-1}$)	2.2×10^{-31}	0	0
Auger Hole Recombination Coefficient ($cm^6\ s^{-1}$)	9.9×10^{-32}	0	0

4.3 Defects in Polycrystalline silicon

In the previous chapter, the amorphous silicon used was obtained from AFORS-HET's material library. This contains information on defect densities in the layers, including band-tails. The library, however, does not contain polycrystalline silicon. While most other parameters were derived from crystalline silicon, under the assumption that the layers are thin enough that intra-grain vertical transport is the dominant[76], the additional defects/traps introduced due to the grain boundaries are essential to consider for realistic V_{OC} estimates.

Fortunately, there is sufficient literature on defect states in polycrystalline silicon from the thin-film transistors community. In this work, I have used trap densities from King et al. for both poly-Si layers, as shown in Fig. 26[77].

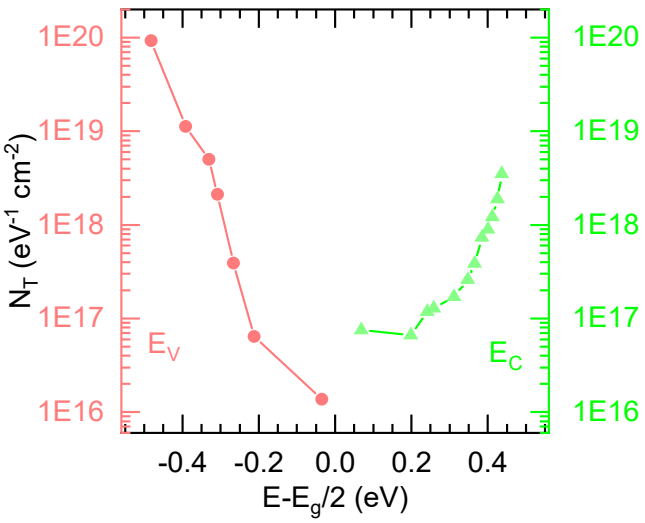

Fig. 26 Trap states as a function of energy in poly-Si extracted from King et al.,[77] using WebPlotDigitizer[78].

4.4 Si/SiO_x interface defects

It is not uncommon to observe significant defect densities compared to bulk at the interface of thermally grown oxide and crystalline silicon[79], which can lead to increased recombination at the interface. To avoid unrealistically high open circuit voltages, it is

important to introduce these trap states at the interface. However, introducing a high trap density at the interface leads to instability in convergence of the model. To overcome this, 0.5 nm thick crystalline silicon layers were added on either side of the absorber with increased defect density to act as defective interface layers, similar to an approach used by Quan et al.[80]. In this work, a defect density of $2 \times 10^{16}\ eV^{-1}cm^{-3}$ was used at the midgap of silicon, corresponding to an areal defect density of $10^{10}\ eV^{-1}cm^{-2}$ for the Si/SiO_x interface which is not unrealistic[81].

4.5 Silicon Oxide Tunneling Barrier Height

The solar cells being discussed in this chapter use silicon oxide for passivation of the absorber. Due to its wide bandgap, however, silicon oxide is an insulator and does not allow drift or diffusive transport. Using a sufficiently thin layer of the oxide can still allow Fowler-Nordheim tunneling between the absorber and the contact[82,83]. At a given temperature, the probability of tunneling decreases with increasing thickness of the tunneling dielectric and the height of the tunneling barrier. While the actual relation of the Fowler-Nordheim transmission probabilities is expressed in terms of Airy functions and is complicated, it is approximately related inverse exponentially with barrier height and tunneling thickness[84]. Therefore, it is important to have a good estimate of the correct barrier height for accurate tunneling.

For electrons, when tunneling from c-Si to poly-Si through the oxide, the barrier height is simply given by the conduction band offset between the semiconductor and the oxide. This can easily be calculated from the difference in electron affinities of the two layers.

$$\Delta\Phi_{B,e} = \Delta E_C = \chi_{Si} - \chi_{SiO_x} \tag{22}$$

For the tunneling of holes, the valence band offset can be calculated from the conduction band offset and the bandgaps of the layers, as shown in equation (23).

$$\Delta\Phi_{B,h} = \Delta E_V = E_{g,SiO_x} - E_{g,Si} - \Delta E_C \tag{23}$$

The bandgap of amorphous silicon oxide assumed in the simulation is 8.9 eV, and its electron affinity is 1 eV. Using these, we see that theoretically, at equilibrium, the barrier height for electrons is, $\Delta\Phi_{B,e} = 3.05\ eV$, and for holes is, $\Delta\Phi_{B,h} = 4.76\ eV$.

Practically, however, the barrier heights seen by the tunneling carriers are lower than those theoretically predicted[85]. While there is no clear consensus in literature on the exact magnitude of the lowering[86–90], in this work, a barrier height of 1 eV was used for both electrons and holes. To maintain this barrier height for both electrons at the front oxide and holes at the rear, their effective band gaps and electron affinities were adjusted, as shown in the band diagram in Fig. 27.

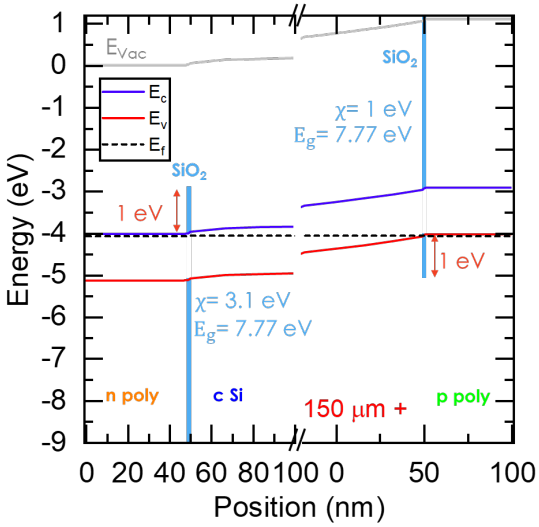

Fig. 27 Band diagram showing oxide band parameters resulting in a 1 eV effective tunneling barrier.

The lowered barrier height has the effect of also allowing easy thermionic emission of both carriers across the junction. This, however, is not practically observed because the true barrier heights for thermionic emission remain high. To suppress this effect, Richardson's constant of the oxide layers was decreased to 0.1 $A\ cm^{-2}K^{-2}$.

4.6 Simulated Cell Results

The current-voltage characteristics of the simulated device using 1.2 nm thick oxide layers are shown in Fig. 28. This is a reasonably realistic representation of an experimental double-side tunnel-oxide solar cell with poly-Si contacts fabricated at NREL, Colorado[75]. While the V_{OC} of the simulation matches exceptionally well with the experimental cell, the simulation overestimates the J_{SC}. This is because the practical cell has significant optical loss due to shading from the front metallization, which is not accounted for in the simulation. Moreover, the experimental cell has higher shunt resistance and, therefore, lower fill factor than the simulated cell.

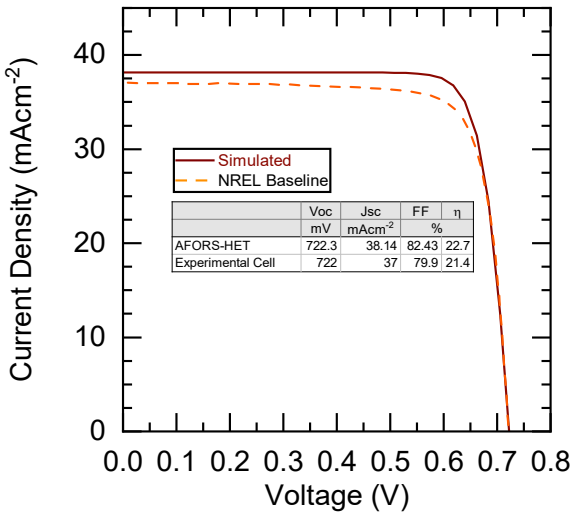

Fig. 28 The JV characteristics of the simulated cell compared to a cell of identical structure courtesy of Dr. Pauls Stradins and Dr. David Young of NREL, Colorado.

4.7 Variation of Oxide Thickness

As discussed in section 4.5, the tunneling probability decreases with increasing thickness of the oxide. Fig. 29 shows that at low oxide thicknesses, performance is invariant. However, increasing the oxide thickness beyond 1.2 nm causes the fill factor to decrease. This is because the contact resistance increases with decreasing tunneling probability. Therefore, it is ideal to have a minimum possible thickness of the oxide. However, low oxide thicknesses have been observed to result in a poorly passivated absorber surfaces[91]. Therefore, typical tunneling oxide based solar cells use a SiO_x thickness of 1.2 nm, which will be used for subsequent discussions.

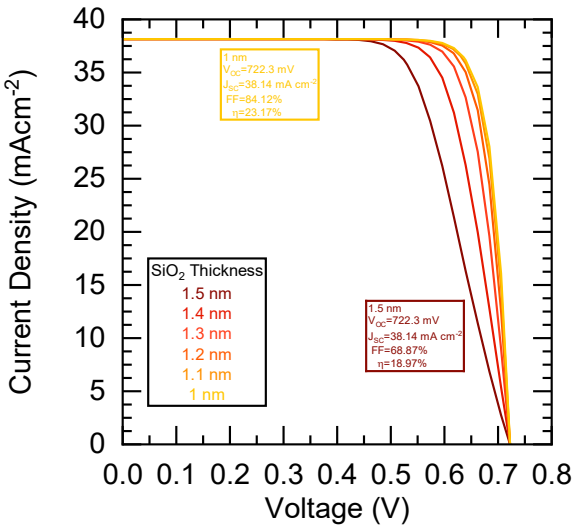

Fig. 29 Current-voltage characteristics for different oxide thicknesses.

4.8 Application of the Model: ITO as an Electron Contact

The thick doped poly-Si contact used in the discussion so far contributes significantly to parasitic absorption in the front. This leaves scope for improved optical performance by the replacement of the front poly-Si layer with a material of wider bandgap and lower absorptance. In 2014, Young et al. proposed the use of ITO as a dopant-free electron

contact to replace the front n-type poly-Si[92]. It was suggested that ITO could provide the correct work function to perform as an electron selective contact. This section investigates the viability of such a contact through simulations.

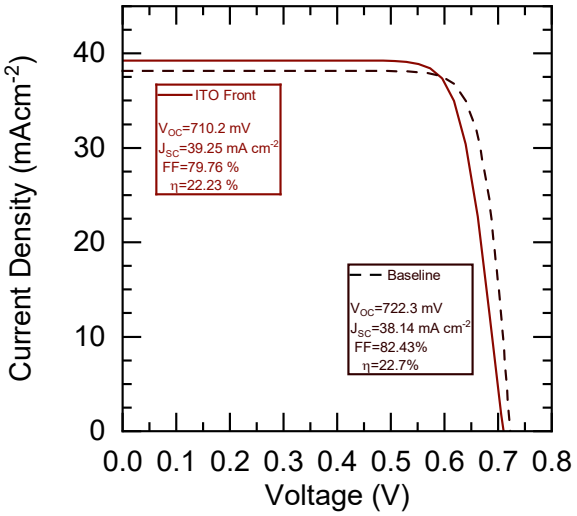

Fig. 30 JV characteristics of the cell using the ITO front contact

Since AFORS-HET does not support degenerate semiconductors, the ITO had to be treated as a front metallization layer, with the only input being its work function. For an initial simulation, a work function of 4.2 eV was used. Fig. 30 shows that the cell with the ITO contact does have better J_{SC} than the simulation of the baseline tunnel-oxide cell. However, it also has a lower open circuit voltage and fill factor. The fill factor is likely affected by the increased series resistance and can depend on the work function of the ITO. Changing the work function of the ITO will also affect the selectivity of the contact, and therefore the V_{OC}. Fig. 31 shows the dependence of solar cell performance on the work function of ITO.

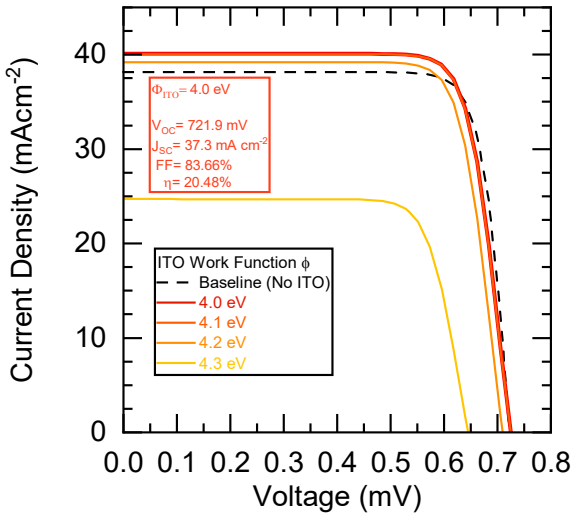

Fig. 31 JV curves for different ITO work functions.

We see that the performance of the solar cell is invariant and better than the baseline cell for work functions of 4.1 eV and below. For work functions above 4.2 eV, however, the fill factor decreases sharply due to decreased selectivity of the ITO contact. Specifically, at 4.2 eV, the ITO is in flat-band condition with the absorber, and above it, the contact becomes electron blocking. It is also observed that the short circuit current decreases with increasing ITO work function. This is likely an artifact arising from the treatment of ITO as a metal instead of a degenerately doped semiconductor.

4.2 eV is close to the lowest practically achievable work functions of ITO. This suggests that such a contact may be possible with other similar TCOs with lower work functions like AZO[93]. However, these materials are deposited through sputtering, which can damage the oxide and deteriorate passivation. Overcoming these challenges can make TCOs a strong contender for low parasitic absorption dopant-free contacts.

4.9 Application of the Model: Buried Doped Regions

Classically, double-side tunnel-oxide cells use a heavily boron-doped poly-Si hole contact at the rear of the cell. This layer is usually deposited as amorphous silicon and then annealed at over 800 °C to recrystallize it[94]. These temperatures are high enough to cause significant diffusion of boron in the poly-Si layer[95]. Boron can easily diffuse through the oxide layer into the crystalline silicon absorber, resulting in a buried layer of boron dopants[25].

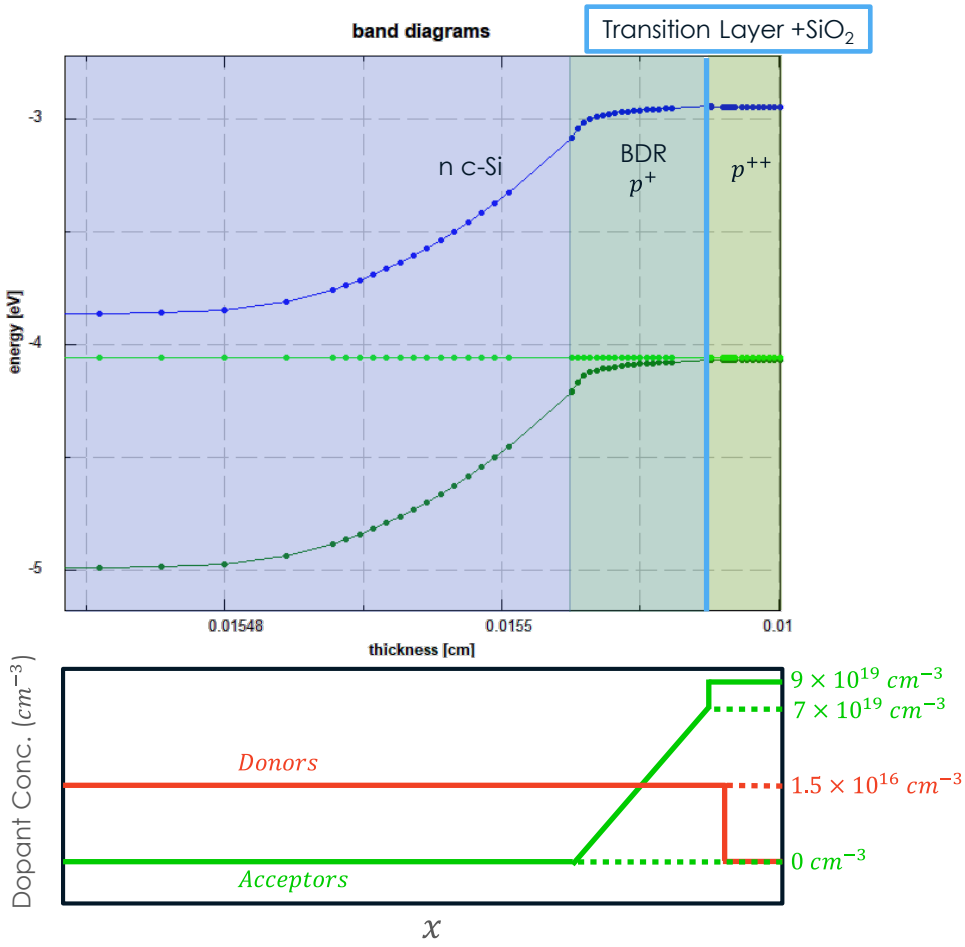

Fig. 32 Simulated band diagram of the buried doped region and schematic of the doping concentration gradient in the layer.

In the solar cell model used in section 4.6, 100 nm of the c-Si absorber was replaced with a buried doped region (BDR). The doping in this region was defined to be a linear gradient from $0\,\mathrm{cm}^{-3}$ to $7\times10^{19}\,\mathrm{cm}^{-3}$ of acceptors over the $1.5\times10^{16}\,\mathrm{cm}^{-3}$ background donor doping of the absorber, as shown in Fig. 32. Also, to simulate damage to passivation, $1\times10^{16}\ cm^{-3}eV^{-3}$ traps were added at mid-gap in this layer.

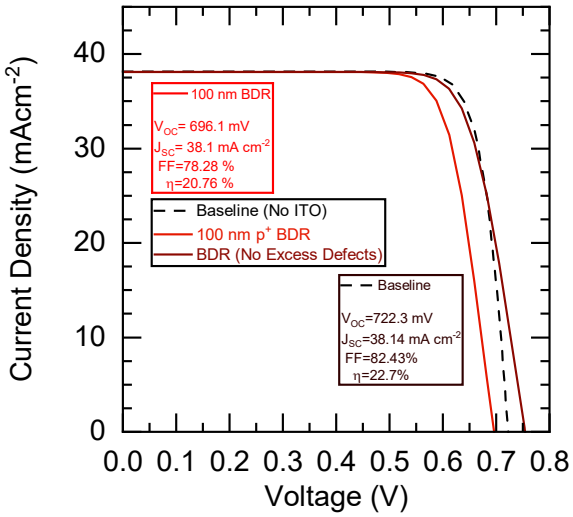

Fig. 33 JV characteristics of the solar cell with a simulated BDR compared to the baseline cell.

From Fig. 33, we see that there is a substantial decrease in V_{OC} for the cell with the buried doped region, as compared to the baseline device. This arises due to the increased defect density in the BDR. Removing these additional defects shows an increase in the V_{OC} because the BDR acts as part of the contact, thereby increasing the contact's selectivity. Realistically, however, the latter effect is dwarfed by the increased recombination arising from the deteriorated passivation. Regardless, there is a decrease in fill factor in both cases. This likely occurs because of the inversion of doping in the BDR.

4.10 Conclusions

In this chapter, an experimentally consistent model of a double-side tunneling oxide passivated solar cell was made in AFORS-HET. This model overestimated the short circuit current slightly, but that can be overcome either by adjusting the generation profile in the solar cell (by changing the illumination) or by using a front surface absorption curve consistent with the increased shading from the front metallization. Despite the shortcomings, this model forms a good basis for understanding the effect of change in device structure on performance. The developed model allows for drop-in replacement of one or more layers. This was exemplified through the analysis of ITO as a replacement for n-doped poly-Si. It was shown that a TCO of work function below 4.2 eV would result in a selective contact, which suggests the viability of AZO as a potential alternative.

The effect of diffused buried doped regions in this kind of device structure was also investigated. While such regions can increase contact selectivity, the increased recombination induced by the boron diffusion causes an overall deterioration of device performance. Thus, this model can also be used to investigate the results of material property changes arising from processing or operation.

CHAPTER 5

CONCLUSIONS

The efficiencies of silicon solar cells today are limited by the ability of contacts to separate charge carriers and prevent recombination. The trifecta of passivating, selective, and conductive contacts is difficult to achieve without a strong understanding of how contacts behave under device operation. In this thesis, I have explored the physics of passivating and selective contacts through simulation of solar cells.

The partial specific contact resistance framework developed by Onno et al. already provided deep insights into the behavior of contacts at open circuit. This work extended the scope of the model to the maximum power point, i.e., the operating point of the solar cell. The equations developed in *chapter 2* allow the calculation of partial specific contact resistances at any current-flow of the device. This means that it is possible to calculate these resistances using simple, measurable device operation inputs like JV and iJV curves. It was shown that the resistances calculated using the equations were generally consistent with those obtained directly from band diagrams, and the prediction error was immaterial to the device's performance. The errors were significant only in the cells with extremely poor selectivity. Since the implied voltage of the device changes negligibly because the slow of current is extremely low, the error in predicting the resistances is limited by the least count or resolution of measurement of the implied voltage. Regardless, this method is applicable for the calculation of partial specific contact resistances of practical solar cells.

The partial specific contact resistance framework is a top-down approach because it helps calculate fundamental device parameters from solar cell performance metrics. While

the framework is useful in understanding contact performance, it is insufficient in predicting the effects of device structure or material changes to overall solar cell performance. Therefore bottom-up solar cell simulation programs like AFORS-HET, which take device structure and material properties as input and predict solar cell performance, are useful.

In this thesis, AFORS-HET was used to understand silicon heterojunction cells with amorphous silicon contacts and silicon oxide passivated solar cells. In both cases, solar cell models were built using practical material properties and commonly used device structures. The performances of the simulated devices were found to be consistent with experiments. For the SHJ cells, the hole contact was replaced with p-$Al_{0.8}Ga_{0.2}As$, with material properties obtained from literature. It was evident that making changes to band alignment by tuning material properties will affect contact performance in terms of majority carrier selectivity, minority carrier blocking, and contact resistance.

For the tunnel-oxide based cells, the poly-Si electron contact was replaced with ITO, and the effect of the ITO work function on its performance as a contact was investigated. It was observed that work function affects the selectivity of the device and hence the $V_{OC.}$ Specifically, the contact is selective when the work function of the contact is below 4.1 eV. This model was also used to understand the behavior of buried doped regions in the absorber that occur due to boron diffusion. These regions can increase the selectivity of the hole contact but damage passivation, thus decreasing overall cell V_{OC}.

Up and coming materials like substoichiometric TCOs, wide bandgap III-Vs and other dopant-free high and low work function materials present compelling alternatives to

silicon-based contacts. Their properties and effect on solar cell performance, however, are not well understood. Thus, the models and tools presented in this thesis present a framework for understanding novel contacts in solar cells.

REFERENCES

1. SolarPower Europe. Global Market Outlook for Solar Power 2020-2024. (2020).

2. Lazard. *Lazard's levelized cost of energy analysis (V 13.0)*. (2019).

3. Jäger-Waldau, A. *PV Status Report 2019*. *Publications Office of the European Union* (2019). doi:10.2760/326629

4. ITRPV. International Technology Roadmap for Photovoltaic 2019. *ITRPV* 76 (2020).

5. Slade, A. & Garboushian, V. 27.6% Efficient Silicon Concentrator Solar Cells for Mass Production. *Tech. Dig. 15th Int. …* 1–2 (2005).

6. Allen, T. G., Bullock, J., Yang, X., Javey, A. & De Wolf, S. Passivating contacts for crystalline silicon solar cells. *Nat. Energy* **4**, 914–928 (2019).

7. Yoshikawa, K. *et al.* Exceeding conversion efficiency of 26% by heterojunction interdigitated back contact solar cell with thin film Si technology. *Sol. Energy Mater. Sol. Cells* **173**, 37–42 (2017).

8. Holman, Z. C. *et al.* Current losses at the front of silicon heterojunction solar cells. *IEEE J. Photovoltaics* **2**, 7–15 (2012).

9. Green, M. A. Self-consistent optical parameters of intrinsic silicon at 300 K including temperature coefficients. *Sol. Energy Mater. Sol. Cells* **92**, 1305–1310 (2008).

10. Gueymard, C. A. SMARTS2: a simple model of the atmospheric radiative transfer of sunshine: algorithms and performance assessment. *Rep. No. FSEC-PF-270-95* 1–84 (1995).

11. Bullock, J., Cuevas, A., Allen, T. & Battaglia, C. Molybdenum oxide MoOx: A versatile hole contact for silicon solar cells. *Appl. Phys. Lett.* **105**, (2014).

12. Bullock, J. *et al.* Lithium Fluoride Based Electron Contacts for High Efficiency n-Type Crystalline Silicon Solar Cells. *Adv. Energy Mater.* **6**, 1–7 (2016).

13. Yang, X. *et al.* High-Performance TiO2-Based Electron-Selective Contacts for Crystalline Silicon Solar Cells. *Adv. Mater.* **28**, 5891–5897 (2016).

14. Matsui, T., Bivour, M., Ndione, P., Hettich, P. & Hermle, M. Investigation of atomic-layer-deposited TiOx as selective electron and hole contacts to crystalline silicon. *Energy Procedia* **124**, 628–634 (2017).

15. Meier, D. L. D. L. & Schroder, D. K. D. K. Contact resistance: Its measurement and relative importance to power loss in a solar cell. *IEEE Trans. Electron Devices* **31**, 647–653 (1984).

16. Cuevas, A. & Yan, D. Misconceptions and misnomers in solar cells. *IEEE J. Photovoltaics* **3**, 916–923 (2013).

17. Fell, A. *et al.* Adaption of basic Metal-Insulator-Semiconductor (MIS) theory for passivating contacts within numerical solar cell modeling. *IEEE J. Photovoltaics* **8**, 1546–1552 (2018).

18. Onno, A., Chen, C., Koswatta, P., Boccard, M. & Holman, Z. C. Passivation, conductivity, and selectivity in solar cell contacts: Concepts and simulations based on a unified partial-resistances framework. *J. Appl. Phys.* **126**, 1–27 (2019).

19. Brendel, R. & Peibst, R. Contact Selectivity and Efficiency in Crystalline Silicon Photovoltaics. *IEEE J. Photovoltaics* **6**, 1413–1420 (2016).

20. Roe, E. T., Egelhofer, K. E. & Lonergan, M. C. Limits of Contact Selectivity/Recombination on the Open-Circuit Voltage of a Photovoltaic. *ACS Appl. Energy Mater.* **1**, 1037–1046 (2018).

21. De Nicolás, S. M., Muñoz, D., Ozanne, A. S., Nguyen, N. & Ribeyron, P. J. Optimisation of doped amorphous silicon layers applied to heterojunction solar cells. *Energy Procedia* **8**, 226–231 (2011).

22. Saive, R. S-Shaped Current–Voltage Characteristics in Solar Cells: A Review. *IEEE J. Photovoltaics* 1–8 (2019). doi:10.1109/jphotov.2019.2930409

23. Varache, R. *et al.* Investigation of selective junctions using a newly developed tunnel current model for solar cell applications. *Sol. Energy Mater. Sol. Cells* **141**, 14–23 (2015).

24. Feldmann, F. *et al.* Tunnel oxide passivated contacts as an alternative to partial rear contacts. *Sol. Energy Mater. Sol. Cells* **131**, 46–50 (2014).

25. Procel, P., Löper, P., Crupi, F., Ballif, C. & Ingenito, A. Numerical simulations of hole carrier selective contacts in p-type c-Si solar cells. *Sol. Energy Mater. Sol. Cells* **200**, 109937 (2019).

26. Würfel, P. *Physics of Solar Cells: From Principles to New Concepts*. *Physics of Solar Cells: From Principles to New Concepts* (2007). doi:10.1002/9783527618545

27. Cuevas, A. *et al.* Skin care for healthy silicon solar cells. *2015 IEEE 42nd Photovolt. Spec. Conf. PVSC 2015* (2015). doi:10.1109/PVSC.2015.7356379

28. Wurfel, U., Cuevas, A. & Wurfel, P. Charge carrier separation in solar cells. *IEEE J. Photovoltaics* **5**, 461–469 (2015).

29. Battaglia, C., Cuevas, A. & De Wolf, S. High-efficiency crystalline silicon solar cells: Status and perspectives. *Energy Environ. Sci.* **9**, 1552–1576 (2016).

30. Taguchi, M. *et al.* HIT cells - High-efficiency crystalline Si cells with novel structure. *Prog. Photovoltaics Res. Appl.* **8**, 503–513 (2000).

31. Santbergen, R. *et al.* GenPro4 Optical Model for Solar Cell Simulation and Its Application to Multijunction Solar Cells. *IEEE J. Photovoltaics* **7**, 919–926 (2017).

32. Ruppel, W. & Würfel, P. Upper Limit for the Conversion of Solar Energy. *IEEE Trans. Electron Devices* **27**, 877–882 (1980).

33. Shockley, W. & Read, W. T. Statistics of the recombinations of holes and electrons. *Phys. Rev.* **87**, 835–842 (1952).

34. Hall, R. N. Electron-hole recombination in germanium [21]. *Physical Review* **87**, 387 (1952).

35. Auger, P. Sur les rayons beta secondaries produits dans gaz par des rayons X. *C.R.A.S.* **177**, 169–171 (1923).

36. Glunz, S. W. *et al.* Passivating and Carrier-selective Contacts - Basic Requirements and Implementation. 2064–2069 (2018). doi:10.1109/pvsc.2017.8366202

37. Mizsei, J. Fermi-level pinning and passivation on the oxide-covered and bare silicon surfaces and interfaces. *Vacuum* **67**, 59–67 (2002).

38. Schmidt, J., Peibst, R. & Brendel, R. Surface passivation of crystalline silicon solar cells: Present and future. *Sol. Energy Mater. Sol. Cells* **187**, 39–54 (2018).

39. Bonilla, R. S., Hoex, B., Hamer, P. & Wilshaw, P. R. Dielectric surface passivation for silicon solar cells: A review. *Phys. Status Solidi Appl. Mater. Sci.* **214**, (2017).

40. Green, M. A. Radiative efficiency of state-of-the-art photovoltaic cells. *Prog. Photovoltaics Res. Appl.* **20**, 472–476 (2012).

41. Haug, H. & Greulich, J. PC1Dmod 6.2 - Improved Simulation of c-Si Devices with Updates on Device Physics and User Interface. *Energy Procedia* **92**, 60–68 (2016).

42. Clugston, D. A. & Basore, P. A. PC1D version 5: 32-bit solar cell modeling on personal computers. *Conf. Rec. IEEE Photovolt. Spec. Conf.* 207–210 (1997). doi:10.1109/pvsc.1997.654065

43. MATLAB. MATLAB. (2018).

44. Altermatt, P. P. Models for numerical device simulations of crystalline silicon solar cells - A review. *J. Comput. Electron.* **10**, 314–330 (2011).

45. De Wolf, S., Descoeudres, A., Holman, Z. C. & Ballif, C. High-efficiency Silicon Heterojunction Solar Cells: A Review. *green* **2**, (2012).

46. Pankove, J. I. & Tarng, M. L. Amorphous silicon as a passivant for crystalline silicon. *Appl. Phys. Lett.* **34**, 156–157 (1979).

47. Leilaeioun, A. (Mehdi) *et al.* Contact resistance of the p-type amorphous silicon hole contact in silicon heterojunction solar cells. *(in Prep.* **85287**,

48. De Wolf, S. & Kondo, M. Nature of doped a-Si:H/c-Si interface recombination. *J. Appl. Phys.* **105**, 103707 (2009).

49. Korte, L. & Schmidt, M. Investigation of gap states in phosphorous-doped ultra-thin a-Si:H by near-UV photoelectron spectroscopy. *J. Non. Cryst. Solids* **354**, 2138–2143 (2008).

50. Filipic, M. *et al.* Amorphous silicon/crystalline silicon heterojunction solar cells-Analysis of lateral conduction through the inversion layer. *Proc. Int. Conf. Microelectron. ICM* 227–230 (2014). doi:10.1109/MIEL.2014.6842128

51. Klein, A. *et al.* Transparent Conducting Oxides for Photovoltaics: Manipulation of Fermi Level, Work Function and Energy Band Alignment. *Materials (Basel).* **3**, 4892–4914 (2010).

52. Zhao, L., Zhou, C. L., Li, H. L., Diao, H. W. & Wang, W. J. Design optimization of bifacial HIT solar cells on p-type silicon substrates by simulation. *Sol. Energy Mater. Sol. Cells* **92**, 673–681 (2008).

53. Bivour, M., Reichel, C., Hermle, M. & Glunz, S. W. Improving the a-Si:H(p) rear emitter contact of n-type silicon solar cells. *Sol. Energy Mater. Sol. Cells* **106**, 11–16 (2012).

54. De Wolf, S. & Kondo, M. Boron-doped a-Si:Hc-Si interface passivation: Degradation mechanism. *Appl. Phys. Lett.* **91**, 1–4 (2007).

55. Kirner, S. *et al.* The Influence of ITO Dopant Density on J-V Characteristics of Silicon Heterojunction Solar Cells: Experiments and Simulations. *Energy Procedia* **77**, 725–732 (2015).

56. Froitzheim, A., Stangl, R., Elstner, L., Kriegel, M. & Fuhs, W. AFORS-HET: A

computer-program for the simulation of hetero-junction solar cells to be distributed for public use. *Proc. 3rd World Conf. Photovolt. Energy Convers.* **A**, 279–282 (2003).

57. Reif, F. & Scott, H. L. Fundamentals of Statistical and Thermal Physics. *Am. J. Phys.* **66**, 164–167 (1998).

58. Schroder, D. K. D. K. & Meier, D. L. D. L. Solar Cell Contact Resistance—A Review. *IEEE Trans. Electron Devices* **31**, 637–647 (1984).

59. Richter, A., Werner, F., Cuevas, A., Schmidt, J. & Glunz, S. W. Improved parameterization of Auger recombination in silicon. in *Energy Procedia* **27**, 88–94 (Elsevier Ltd, 2012).

60. Manzoor, S., Filipič, M., Onno, A., Topič, M. & Holman, Z. C. Visualizing light trapping within textured silicon solar cells. *J. Appl. Phys.* **127**, (2020).

61. PV Lighthouse. PV Lighthouse: SunSolve^{TM}. Available at: https://www.pvlighthouse.com.au. (Accessed: 10th October 2020)

62. Leilaeioun, M. A. *et al.* Power Losses in the Front Transparent Conductive Oxide Layer of Silicon Heterojunction Solar Cells: Design Guide for Single-Junction and Four-Terminal Tandem Applications. *IEEE J. Photovoltaics* **10**, 326–334 (2020).

63. Bett, A. W., Dimroth, F., Stollwerck, G. & Sulima, O. V. III-V compounds for solar cell applications. *Appl. Phys. A Mater. Sci. Process.* **69**, 119–129 (1999).

64. Epple, J. H. *et al.* Formation of highly conductive polycrystalline GaAs from annealed amorphous (Ga,As). *J. Appl. Phys.* **93**, 5331–5336 (2003).

65. Knights, J. C. & Lujan, R. A. Plasma deposition of GaP and GaN. *J. Appl. Phys.* **49**, 1291–1293 (1978).

66. O'Reilly, E. P. & Robertson, J. Electronic structure of amorphous III-V and II-VI compound semiconductors and their defects. *Phys. Rev. B* **34**, 8684–8695 (1986).

67. Yao, Y. *et al.* Optical and Electrical Properties of a-InGaAs : H Films Prepared by Double-Target Magnetron Co-sputtering. in *2008 2nd IEEE International Nanoelectronics Conference, INEC 2008* 411–414 (IEEE, 2008). doi:10.1109/INEC.2008.4585517

68. Matsumoto, N. & Kumabe, K. Effects of Hydrogen Incorporation during Deposition by Sputtering for Amorphous Gallium Phosphide Films. *Jpn. J. Appl. Phys.* **18**, 1011–1012 (1979).

69. Hajakbari, F., Larijani, M. M., Ghoranneviss, M., Aslaninejad, M. & Hojabri, A. Optical Properties of Amorphous AlN Thin Films on Glass and Silicon Substrates Grown by Single Ion Beam Sputtering. *Jpn. J. Appl. Phys.* **49**, 095802 (2010).

70. Tiedje, T., Yablonovitch, E., Cody, G. D. & Brooks, B. G. Limiting Efficiency of Silicon Solar Cells. *IEEE Trans. Electron Devices* **31**, 711–716 (1984).

71. Beyer, W. & Wagner, H. Determination of the hydrogen diffusion coefficient in hydrogenated amorphous silicon from hydrogen effusion experiments. *J. Appl. Phys.* **53**, 8745–8750 (1982).

72. Mazzarella, L. *et al.* Optimization of PECVD process for ultra-thin tunnel SiO x film as passivation layer for silicon heterojunction solar cells. *2017 IEEE 44th Photovolt. Spec. Conf. PVSC 2017* 1–5 (2017). doi:10.1109/PVSC.2017.8366698

73. Feldmann, F. *et al.* A Passivated Rear Contact for High-Efficiency n-Type Si Solar Cells Enabling High Voc's and FF>82 %. *28th Eur. Photovolt. Sol. Energy Conf. Exhib.* (2013). doi:10.4229/28thEUPVSEC2013-2CO.4.4

74. Feldmann, F., Reichel, C., Müller, R. & Hermle, M. The application of poly-Si/SiOx contacts as passivated top/rear contacts in Si solar cells. *Sol. Energy Mater. Sol. Cells* **159**, 265–271 (2017).

75. Young, D. L. *et al.* Front/Back Poly-Si/SiO2 Passivated Contact Device with Voc > 720 mV. in *35th European Photovoltaic Solar Energy Conference and Exhibition* 700–703 (2018). doi:10.4229/35thEUPVSEC20182018-2AV.3.32

76. Teodoreanu, A. M., Leendertz, C., Sontheimer, T., Korte, L. & Rech, B. An effective medium approach for modeling polycrystalline silicon thin film solar cells. *Sol. Energy Mater. Sol. Cells* **117**, 152–160 (2013).

77. King, T. J., Hack, M. G. & Wu, I. W. Effective density-of-states distributions for accurate modeling of polycrystalline-silicon thin-film transistors. *J. Appl. Phys.* **75**, 908–913 (1994).

78. Rohatgi, A. WebPlotDigitizer. (2020).

79. Stathis, J. H., Buchanan, D. A., Quinlan, D. L., Parsons, A. H. & Kotecki, D. E. Interface defects of ultrathin rapid-thermal oxide on silicon. *Appl. Phys. Lett.* **62**, 2682–2684 (1993).

80. Quan, C. *et al.* Computational analysis of a high-efficiency tunnel oxide passivated contact (TOPCon) solar cell with a low-work-function electron-selective-collection layer. *Sol. Energy* **170**, 780–787 (2018).

81. Johnson, N. M., Biegelsen, D. K. & Moyer, M. D. CHARACTERISTIC DEFECTS AT THE Si-SiO2 INTERFACE. *Phys. MOS Insul.* 311–315 (1980). doi:10.1016/b978-0-08-025969-7.50064-6

82. Fowler, R. H. & Nordheim, L. -Electron Emission in Intense Fields - Nordheim & Fowler. **5**, (1928).

83. Ravindra, N. M. & Zhao, J. Fowler-Nordheim tunneling in thin SiO 2 films. *Smart Mater. Struct.* **1**, 197–201 (1992).

84. Wolters, D. R. & Zegers-Van Duijnhoven, A. T. A. Tunnelling in thin SiO2. *Philos. Trans. R. Soc. A Math. Phys. Eng. Sci.* **354**, 2327–2350 (1996).

85. Gan, J.-Y. Polysilicon emitters for silicon concentrator solar cells. (Stanford University, 1990).

86. Glunz, S. W. & Feldmann, F. SiO2 surface passivation layers – a key technology for silicon solar cells. *Sol. Energy Mater. Sol. Cells* **185**, 260–269 (2018).

87. Post, I. R. C. & Ashburn, P. Investigation of Boron Diffusion in Polysilicon and its Application to the Design of P-N-P Polysilicon Emitter Bipolar Transistors with Shallow Emitter Junctions. *IEEE Trans. Electron Devices* **38**, 2442–2451 (1991).

88. Maritan, C. M. Poly silicon Emitter p-n-p Transistors. **36**, (1989).

89. Kasprzak, L. A., Laibowitz, R. B. & Ohring, M. Dependence of the Si-SiO2 barrier height on SiO2 thickness in MOS tunnel structures. *J. Appl. Phys.* **48**, 4281–4286 (1977).

90. Liebhaber, M. *et al.* Valence band offset and hole transport across a-SiOx ($0<x<2$) passivation layers in silicon heterojunction solar cells. *EUPVSEC* **107**, 608498 (2015).

91. Kale, A. S. *et al.* Effect of silicon oxide thickness on polysilicon based passivated contacts for high-efficiency crystalline silicon solar cells. *Sol. Energy Mater. Sol. Cells* **185**, 270–276 (2018).

92. Young, D. L. *et al.* Carrier Selective, Passivated Contacts for High Efficiency Silicon Solar Cells based on Transparent Conducting Oxides. *Energy Procedia* **55**, 733–740 (2014).

93. Morales-Masis, M., De Wolf, S., Woods-Robinson, R., Ager, J. W. & Ballif, C. Transparent Electrodes for Efficient Optoelectronics. *Adv. Electron. Mater.* **3**, (2017).

94. Tao, Y., Upadhyaya, V., Jones, K. & Rohatgi, A. Tunnel oxide passivated rear contact for large area n-type front junction silicon solar cells providing excellent carrier selectivity. *AIMS Mater. Sci.* **3**, 180–189 (2016).

95. Shao, L., Liu, J., Chen, Q. Y. & Chu, W. K. *Boron diffusion in silicon: The anomalies and control by point defect engineering*. *Materials Science and Engineering R: Reports* **42**, (2003).